

Coordinated Science Laboratory

AD-A227 487

DTIC FILE COPY

**TWO-DIMENSIONAL
SIMULATION OF
QUANTUM-WELL LASERS
INCLUDING
ENERGY TRANSPORT**

Ghie Hugh Song

DTIC
ELECTE
OCT 09 1990
S E D
G

College of Engineering

UNIVERSITY OF ILLINOIS AT URBANA-CHAMPAIGN

Approved for Public Release. Distribution Unlimited.

90 10 05 003

REPORT DOCUMENTATION PAGE				Form Approved OMB No. 0704-0188	
1a. REPORT SECURITY CLASSIFICATION Unclassified			1b. RESTRICTIVE MARKINGS None		
2a. SECURITY CLASSIFICATION AUTHORITY			3. DISTRIBUTION/AVAILABILITY OF REPORT Approved for public release; distribution unlimited		
2b. DECLASSIFICATION/DOWNGRADING SCHEDULE					
4. PERFORMING ORGANIZATION REPORT NUMBER(S) UIIU-ENG-90-2241			5. MONITORING ORGANIZATION REPORT NUMBER(S)		
6a. NAME OF PERFORMING ORGANIZATION Coordinated Science Lab University of Illinois		6b. OFFICE SYMBOL (if applicable) N/A	7a. NAME OF MONITORING ORGANIZATION Office of Naval Research		
6c. ADDRESS (City, State, and ZIP Code) 1101 W. Springfield Ave. Urbana, IL 61801			7b. ADDRESS (City, State, and ZIP Code) Arlington, VA 22217-5000		
8a. NAME OF FUNDING/SPONSORING ORGANIZATION Office of Naval Research		8b. OFFICE SYMBOL (if applicable)	9. PROCUREMENT INSTRUMENT IDENTIFICATION NUMBER N00014-86-K-0512		
8c. ADDRESS (City, State, and ZIP Code) Arlington, VA 22217-5000			10. SOURCE OF FUNDING NUMBERS		
			PROGRAM ELEMENT NO.	PROJECT NO.	TASK NO.
			WORK UNIT ACCESSION NO.		
11. TITLE (Include Security Classification) TWO-DIMENSIONAL SIMULATION OF QUANTUM-WELL LASERS INCLUDING ENERGY TRANSPORT					
12. PERSONAL AUTHOR(S) Song, G. H.					
13a. TYPE OF REPORT Technical		13b. TIME COVERED FROM _____ TO _____		14. DATE OF REPORT (Year, Month, Day) 1990 August	
15. PAGE COUNT 79					
16. SUPPLEMENTARY NOTATION					
17. COSATI CODES			18. SUBJECT TERMS (Continue on reverse if necessary and identify by block number)		
FIELD	GROUP	SUB-GROUP	quantum-well lasers, energy transport, semiconductor lasers, steady state, transients		
19. ABSTRACT (Continue on reverse if necessary and identify by block number)					
<p>A versatile, two-dimensional simulator for various types of semiconductor lasers for both steady state and transients has been developed. The simulator is capable of spectral analysis of quantum-well semiconductor lasers, such as gain-spectrum analysis, as well as analysis of the two-dimensional current flow and optical intensity patterns. The simulator is based on the drift-diffusion model with full Fermi-Dirac statistics for the transport equations as well as for the Poisson equation. Simulation of the thermionic emission</p>					
(OVER)					
20. DISTRIBUTION/AVAILABILITY OF ABSTRACT <input checked="" type="checkbox"/> UNCLASSIFIED/UNLIMITED <input type="checkbox"/> SAME AS RPT. <input type="checkbox"/> DTIC USERS			21. ABSTRACT SECURITY CLASSIFICATION Unclassified		
22a. NAME OF RESPONSIBLE INDIVIDUAL			22b. TELEPHONE (Include Area Code)		22c. OFFICE SYMBOL

current is required at the abrupt hetero-interfaces of the quantum well. Energy transfer among the charge carriers, crystal lattice, and optical radiation in an optoelectronic semiconductor device is analyzed in order to obtain details of the internal temperature distribution. Fermi-Dirac statistics and the spatial band-gap variation in a degenerate semiconductor device with nonuniform band structure are included in the analysis. Sources of ill-conditioning in the simulation of thermal flow in semiconductor devices are considered, and a new conditioning scheme which gives a satisfactory convergence for the Newton method is also described. The boundary conditions for the energy flow equation are discussed. For the spectral analysis of quantum-well lasers, we have used the photon rate equation for each Fabry-Perot mode. For the optical intensity pattern, we have solved the two-dimensional Helmholtz eigenvalue equation using the subspace iteration method. The transient simulation is done by the backward-Euler method in conjunction with the full Newton approach for the entire semiconductor equations. To demonstrate the simulator, a model GaAs-AlGaAs graded-index-separate-confinement-heterostructure buried-quantum-well laser is analyzed.

TWO-DIMENSIONAL SIMULATION OF QUANTUM-WELL LASERS
INCLUDING ENERGY TRANSPORT

BY

GHIE HUGH SONG

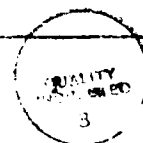
B. S., Seoul National University, 1980
M. S., Korea Advanced Institute of Science, 1982

THESIS

Submitted in partial fulfillment of the requirements
for the degree of Doctor of Philosophy in Electrical Engineering
in the Graduate College of the
University of Illinois at Urbana-Champaign, 1990

Urbana, Illinois

Accession For	
NTIS GRA&I	<input checked="checked" type="checkbox"/>
DTIC TAB	<input type="checkbox"/>
Unannounced	<input type="checkbox"/>
Justification	
By _____	
Distribution/	
Availability Codes	
Dist	Avail and/or Special
A-1	



©Copyright by

Ghie Hugh Song

1990

TWO-DIMENSIONAL SIMULATION OF QUANTUM-WELL LASERS INCLUDING ENERGY TRANSPORT

Ghie Hugh Song, Ph. D.

Department of Electrical and Computer Engineering

University of Illinois at Urbana-Champaign, 1990

K. Hess, Advisor

A versatile, two-dimensional simulator for various types of semiconductor lasers for both steady state and transients has been developed. The simulator is capable of spectral analysis of quantum-well semiconductor lasers, such as gain-spectrum analysis, as well as analysis of the two-dimensional current flow and optical intensity patterns. The simulator is based on the drift-diffusion model with full Fermi-Dirac statistics for the transport equations as well as for the Poisson equation. Simulation of the thermionic emission current is required at the abrupt hetero-interfaces of the quantum well. Energy transfer among the charge carriers, crystal lattice, and optical radiation in an optoelectronic semiconductor device is analyzed in order to obtain details of the internal temperature distribution. Fermi-Dirac statistics and the spatial band-gap variation in a degenerate semiconductor device with nonuniform band structure are included in the analysis. Sources of ill-conditioning in the simulation of thermal flow in semiconductor devices are considered, and a new conditioning scheme which gives a satisfactory convergence for the Newton method is also described. The boundary conditions for the energy flow equation are discussed. For the spectral analysis of quantum-well lasers, we have used the photon rate equation for each Fabry-Perot mode. For the optical intensity pattern, we have solved the two-dimensional Helmholtz eigenvalue equation using the subspace iteration method. The transient simulation is done by the backward-Euler method in conjunction with the full Newton approach for the entire semiconductor equations. To demonstrate the simulator, a model GaAs-AlGaAs graded-index-separate-confinement-heterostructure buried-quantum-well laser is analyzed.

DEDICATION

To My Father

ACKNOWLEDGEMENTS

The author would like to express very special thanks to his advisor, Professor Karl Hess for his invaluable guidance and support in pursuing this project. The author is much obliged to Professors Kyekyoon Kim, Sung M. Lim, and Chester S. Gardner for their thoughtful considerations of him throughout his life at the University of Illinois. He is also grateful to and would like to acknowledge Professors Thomas Kerkhoven, Umberto Ravaioli, James J. Coleman, Shun-Lien Chuang, Jean-Pierre Leburton, Ki D. Lee, and Steve S. Kang of the University of Illinois; Dr. R. Kent Smith of AT&T Bell Laboratories; Dr. Hong K. Choi of MIT Lincoln Laboratories, and Dr. Jeong M. Lim of the Computer Science Department at the University of Illinois for valuable discussions regarding various technical problems in the project. He is thankful to Dr. Frank Stern at IBM in Yorktown Heights for his appreciation and encouragement of the author's work.

The author would also like to thank friends of his family, John and Greta Levis, and his colleagues in the laboratory, Matthew Grupen, Gregory A. Kosinovsky, Albert Galick, Ki W. Kim, and Jack Higman for their assistance and collaboration.

He is obliged to his parents for their strong family support and, most especially to his wife, who has had the burden of sharing all the pains of graduate years.

This work has been supported by the National Science Foundation through the Engineering Research Center of the University of Illinois at Urbana-Champaign and the Office of Naval Research under the SDIO-IST program.

TABLE OF CONTENTS

CHAPTER		PAGE
1	ENERGY FLOW IN A DEGENERATE SEMICONDUCTOR DEVICE WITH NONUNIFORM BAND STRUCTURE AND RADIATION .	1
1.1	Introduction	1
1.2	Conservation of Energy	2
1.3	Analytic Considerations	5
1.3.1	Expressions for the conserved quantities and sources	5
1.3.2	Expressions for fluxes	6
1.3.3	Quantum-well regions	7
1.4	Conditioning the Heat Flow Equation	8
1.5	Discretization of Flux Equations	10
1.6	Boundary Conditions for the Heat Flow Equation	12
2	MINILASE AND TWO-DIMENSIONAL ANALYSIS OF QUANTUM-WELL LASERS	16
2.1	Introduction	16
2.2	Physical Considerations	17
2.3	Modeling of physical Parameters	19
2.3.1	Sources of Poisson equation	19
2.3.2	Hall-Shockley-Reed recombination	20
2.3.3	Auger recombination	20
2.3.4	Radiative recombination	22
2.3.5	Refractive index	26
2.3.6	Free-Carrier absorption and photon lifetime	27
2.3.7	Carrier mobilities of $\text{Al}_x\text{Ga}_{1-x}\text{As}$	28
2.4	Numerical Approach	30
2.5	Application to Quantum-Well Lasers	32
3	CONCLUSIONS	51
	APPENDICES	53
A	ENERGY CONSERVATION FROM THE BOLTZMANN TRANSPORT EQUATION	53
B	EXPRESSIONS FOR THE HEAT FLUX	55
B.1	From Relaxation-Time Approximation	55

B.2 Heat Flux in the Hydrodynamic Model with the Relaxation-Time Approximation	59
C EXPRESSIONS FOR CARRIER FLUX	62
LIST OF REFERENCES	65
VITA	72

CHAPTER 1

ENERGY FLOW IN A DEGENERATE SEMICONDUCTOR DEVICE WITH NONUNIFORM BAND STRUCTURE AND RADIATION

1.1 Introduction

The simulation of heat or energy flow in semiconductor devices is a complex problem. There are three basic models for energy transport: The first one is due to Stratton [1], which represents a good approximation as long as the asymmetric portion of the momentum distribution of carriers is small. The so-called hydrodynamic model due to Bløtekjær [2] is slightly more general but has the disadvantage that several transport coefficients can only be determined by direct solution of the Boltzmann transport equations (BTE). The third is, of course, the direct solution of the BTE by the Monte-Carlo methods, for example. Here we use Stratton's approach with a careful choice of proper expressions for particle and energy or heat fluxes. Expressions for particle fluxes derived from the BTE have been studied extensively [3]–[12].

We begin with a discussion of the coupling of the energy conservation equations for various physical subsystems, including the radiation system, as appropriate for the simulation of optoelectronic semiconductor devices. We examine various mathematically equivalent expressions for their numerical performance in actual simulations. The discretized heat equation often shows signs of an ill-conditioned matrix problem. We investigate causes and cures, and discuss the discretization scheme for various flux expressions.

We consider three types of boundary conditions for the thermal equation: Dirichlet conditions, von Neumann conditions with vanishing energy flux, and heat current boundary condition. In a realistic situation, lead wires are typically used to provide a current

or voltage bias. We also review the adaptability of the various equivalent expressions for particle and energy fluxes, and attempt to clarify physical concepts of heat flux and dissipative energy flux in the energy transport equation. These concepts are often borrowed from classical nonequilibrium thermodynamics and need to be adapted to the electron dynamics in semiconductors.

1.2 Conservation of Energy

We consider four physical systems: the systems of electrons, the holes, the crystal lattice, and the radiation. We then can construct four energy conservation equations for these four systems (Appendix A):

$$\begin{aligned} \partial u_e / \partial t = & -\nabla \cdot \mathbf{S}_e - E_C^+ U_{\text{HSR}} - Q_{e\text{-lat}} \\ & + X_{\text{Aug}} + X_{e\text{-h}} - E_{C,\hbar\omega}^+ U_{\text{rad}} + \hbar\omega R_{e,\text{fc}}, \end{aligned} \quad (1.1)$$

$$\begin{aligned} \partial u_h / \partial t = & -\nabla \cdot \mathbf{S}_h - E_V^- U_{\text{HSR}} - Q_{h\text{-lat}} \\ & + X_{\text{Aug}} + X_{e\text{-h}} - E_{V,\hbar\omega}^- U_{\text{rad}} + \hbar\omega R_{h,\text{fc}}, \end{aligned} \quad (1.2)$$

$$\partial u_{\text{lat}} / \partial t = -\nabla \cdot \mathbf{S}_{\text{lat}} + E_g^+ U_{\text{HSR}} + Q, \quad (1.3)$$

$$\partial u_{\text{rad}} / \partial t = -\nabla \cdot \mathbf{S}_{\text{rad}} + \hbar\omega (U_{\text{rad}} - R^{\text{fc}}), \quad (1.4)$$

$$E_g^+ = E_C^+ - E_V^-, \quad \hbar\omega = E_{C,\hbar\omega}^+ - E_{V,\hbar\omega}^-,$$

$$R^{\text{fc}} = R_e^{\text{fc}} - R_h^{\text{fc}}, \quad Q = Q_{e\text{-lat}} - Q_{h\text{-lat}}.$$

Here t is time, and u_e , u_h , u_{lat} , and u_{rad} are the energy densities for the electron, the hole, the lattice, and the radiation systems, respectively. The vectors, \mathbf{S}_e , \mathbf{S}_h , \mathbf{S}_{lat} , and \mathbf{S}_{rad} are the energy flux densities for the respective systems. The energy flux for the radiation system, \mathbf{S}_{rad} , is also called the Poynting vector in electromagnetics. The symbols, U_{rad} and U_{HSR} , represent the net rates of radiative recombination and Hall-Shockley-Reed recombination, and R_e^{fc} and R_h^{fc} refer to the free-carrier-absorption rate

for electrons and holes, respectively. The energy denoted by E_g^+ , which is slightly larger than the energy band gap E_g , is the average energy released by the Hall-Shockley-Reed recombination or the Auger recombination depending on where it is used. The constant, $\hbar \equiv h/2\pi$, is the Planck constant, and $\hbar\bar{\omega}$ is the average energy released by the radiative recombination. The terms X_{Aug} and X_{e-h} represent the rate of energy exchange due to the Auger recombination and electron-hole scattering, respectively. The terms Q_e and Q_h represent the heat dissipation to the lattice system from the respective carrier systems by the intraband thermal relaxation process. The sources of these terms are the Joule heat, the Peltier heat (at abrupt heterojunctions), and the heat dissipated from excited electrons or holes due to free carrier absorption and the Auger process. The Auger process itself does not involve energy transfer to the lattice system. However, the Auger recombination process, as well as the free-carrier absorption process, leaves an electron in mid-conduction band or a hole in mid-valence band. This carrier then relaxes its energy, giving off heat to the lattice. The energy transferred to the lattice system by this process, as well as the Joule heat, is included in the term Q .

The radiation system and the lattice system can be thought of as sums of energy conservation equations for infinitely many modes. The radiation system is often conveniently represented by the photon rate equations for individual modes after integrating over the space under consideration. Each photon rate equation is of the form

$$\partial S_\nu / \partial t = G_\nu S_\nu + R_\nu^{\text{sp}} - S_\nu / \tau_{\text{ph}}. \quad (1.5)$$

Here τ_ν is the photon lifetime, and S_ν , G_ν and R_ν^{sp} are the photon occupation number, the mode gain, and the spontaneous emission rate of mode ν . Note that the space integration of the Poynting vector has, with that of the free-carrier absorption term, been replaced by S_ν / τ_ν , and that of the optical energy density has been replaced by the sum of S_ν 's.

The lattice system cannot be treated in this way. The anharmonicity of the Hamiltonian creates a coupling of phonon modes resulting in thermodynamically irreversible heat dissipation through Umklapp processes. Energy exchange between the carrier system and

the resonant radiation system (as in a semiconductor laser) maintains the reversibility on short-time scales, resulting in transient "ringing" of radiation mode amplitudes.

The information which we seek to obtain from the heat flow simulation is the internal temperature distribution. If the energy exchange among the various systems is weak, one is forced to introduce individual average energies for electrons, holes, lattices, and photons. If the energy exchange between the electron system and the hole system is fast enough, the average electron and hole energies can be considered equal, and we need only one conservation equation for those two systems with the source term $-\hbar\bar{\omega}(U^{\text{rad}} - R^{\text{fc}}) - E_g^+ U^{\text{HSR}} - Q$. If the energy exchange between the carrier and lattice systems is rapid, we can introduce a temperature which is equal for electrons, holes, and the crystal lattice, and we may combine (1.1)–(1.3) to obtain

$$\frac{\partial}{\partial t}(u_e - u_h + u_{\text{lat}}) = -\nabla \cdot (\mathbf{S}_e - \mathbf{S}_h + \mathbf{S}_{\text{lat}}) - \hbar\bar{\omega}(U^{\text{rad}} - R^{\text{fc}}). \quad (1.6)$$

In doing this we have canceled the heat dissipation term Q for the Joule heat and the hot carrier relaxation, either of which is not easy to realize or have no simple explicit expression for numerical simulation.

In the simulations we also need to include the Poisson equation and the following carrier continuity equations along with energy balance equations.

$$\frac{\partial}{\partial t}\{n, p\} + \nabla \cdot \{\mathbf{j}_e, \mathbf{j}_h\} + U_{\text{rad}} + U_{\text{HSR}} + U_{\text{Aug}} = 0. \quad (1.7)$$

Here n [p] and \mathbf{j}_e [\mathbf{j}_h] are the electron [hole] density and the particle flux density, respectively, and U_{Aug} is the net rate of the Auger recombination. To solve all equations self-consistently, one needs to express the various contributions to those equations in terms of a set of variables which are chosen as the unknowns for the system of equations. These variables are the electrostatic potential, the carrier densities n and p , and the temperature, under the assumption that local equilibrium is maintained so that a local temperature is a valid concept. Instead of n and p , we use η_e and η_h , sometimes called

“Planck potentials” [13] which are defined below. This is advantageous when the heat transfer is involved.

1.3 Analytic Considerations

1.3.1 Expressions for the conserved quantities and sources

There are various expressions available for the various rate terms in (1.5)–(1.7) with varying degrees of approximation, which are described, e.g., in [14].

The conserved quantities in the continuity equations can be expressed in terms of η_e , η_h , and temperature. Assuming a parabolic band structure with density-of-states-equivalent effective masses m_e and m_h for electrons and holes, respectively, one has

$$n = N'_C T^{3/2} \mathcal{F}_{1/2}(\eta_e), \quad p = N'_V T^{3/2} \mathcal{F}_{1/2}(\eta_h), \quad (1.8)$$

$$u_e \simeq N'_C T^{3/2} \left[\frac{3}{2} T \mathcal{F}_{3/2}(\eta_e) + E_C \mathcal{F}_{1/2}(\eta_e) \right], \quad (1.9)$$

$$u_h \simeq N'_V T^{3/2} \left[\frac{3}{2} T \mathcal{F}_{3/2}(\eta_h) - E_V \mathcal{F}_{1/2}(\eta_h) \right], \quad (1.10)$$

$$N'_C = 2 \left(m_e / 2\pi \hbar^2 \right)^{3/2}, \quad N'_V = 2 \left(m_h / 2\pi \hbar^2 \right)^{3/2},$$

$$\eta_e = (F_e - E_C) / T, \quad \eta_h = (E_V - F_h) / T, \quad (1.11)$$

$$E_C = -q\psi - \chi, \quad E_V = E_C - E_G, \quad (1.12)$$

$$\mathcal{F}_j(\eta) = \frac{1}{j!} \int_0^\infty \frac{x^j}{e^{x-\eta} + 1} dx,$$

where F_e and F_h are the quasi-Fermi levels for electrons and holes, respectively, E_C and E_V are the conduction and valence band edges, respectively, and ψ is the electrostatic potential. The variables χ and E_G refer to the electron affinity and bandgap of the material, respectively, and T is the temperature in energy units. Closed-form expressions for the above quantities for nonparabolic band structure are found in [7]. The effect of particle streaming on the carrier densities has been included within the framework of local

quasi-Fermi levels and the local temperatures. However, the effect on the energy densities $\frac{1}{2}m_e^* |\mathbf{j}_e|^2 / n$, which is additional to (1.9), has been ignored by taking the equilibrium Fermi-Dirac functions for the integration over the phase space. This should be of concern as discussed in Appendix A regarding the equation for the conservation of energy.

The energy stored in the lattice is [9]

$$u_{\text{lat}} = \int_0^{\omega_D} \frac{D(\omega)}{e^{\hbar\omega/T} - 1} d\omega, \quad (1.13)$$

where ω_D represents the Debye frequency, and $D(\omega)$ is the density of phonon states. For use in the context of time derivative, the following equation is used [13].

$$\partial u_{\text{lat}} / \partial t = c_P \partial T / \partial t, \quad (1.14)$$

where c_P is the pressure-specific heat capacity per unit volume of the device material.

The expression for each term of $\hbar\bar{\omega} (U^{\text{rad}} - R^{\text{fc}})$ in (1.6), which represents the energy exchange from the stimulated emission, spontaneous emission, and free-carrier absorption, are discussed in Chapter 2.

1.3.2 Expressions for fluxes

In addition to the above rates, expressions for the various fluxes are needed. We assume that the relaxation time of hot carriers is negligibly small on our time scale. Then we can use the linear form of the transport equations derived from the BTE for the particle fluxes in the absence of a magnetic field in a degenerate semiconductor. The particular form of expressions for various fluxes which we use here is most suitable for the case when the carrier degeneracy, band structure nonuniformity, and temperature gradient are important at the same time.

$$\mathbf{j}_e = -M_e [\mathcal{F}_0(\eta_e) (T \nabla \eta_e + \nabla E_C) + 2\mathcal{F}_1(\eta_e) \nabla T], \quad (1.15)$$

$$\mathbf{j}_h = -M_h [\mathcal{F}_0(\eta_h) (T \nabla \eta_h - \nabla E_V) + 2\mathcal{F}_1(\eta_h) \nabla T], \quad (1.16)$$

$$M_e = \mu_e n / q \mathcal{F}_0(\eta_e), \quad M_h = \mu_h p / q \mathcal{F}_0(\eta_h). \quad (1.17)$$

Here μ_e and μ_h are the mobilities of electrons and holes, respectively, and q is the elementary charge. The energy flux expressions which are symmetric in the sense of the Onsager relations [13] are

$$\mathbf{S}_e = E_C \mathbf{j}_e + \mathbf{S}_e^{\text{kin}}, \quad \mathbf{S}_h = E_V \mathbf{j}_h - \mathbf{S}_h^{\text{kin}}, \quad (1.18)$$

$$\mathbf{S}_e^{\text{kin}} = -M_e T [2\mathcal{F}_1(\eta_e) (T \nabla \eta_e + \nabla E_C) + 6\mathcal{F}_2(\eta_e) \nabla T], \quad (1.19)$$

$$\mathbf{S}_h^{\text{kin}} = -M_h T [2\mathcal{F}_1(\eta_h) (T \nabla \eta_h - \nabla E_V) + 6\mathcal{F}_2(\eta_h) \nabla T]. \quad (1.20)$$

The derivation of the above particular forms with an extension to the first-order approximation for the nonparabolic bands is given in Appendix B, along with integral expressions deduced from the BTE.

The heat flux equation for phonons,

$$\mathbf{S}_{\text{lat}} = -\kappa \nabla T, \quad (1.21)$$

can also be used as the expression for the phonon energy flux, with κ being the lattice heat conductivity of the material.

1.3.3 Quantum-well regions

The expressions in (1.8)–(1.12) are used everywhere except in the size-quantized regions. Inside the quantum well, we use

$$n = \frac{T m_e^\Gamma}{\pi^2 \hbar^3 t^q} \sum_l \mathcal{F}_0 \left(\eta_e - \frac{E_{e,l}^{\text{th}}}{T} \right), \quad E_{e,l}^{\text{th}} \simeq \frac{\hbar^2}{2m_e} \left(\frac{l\pi}{t^q} \right)^2, \quad (1.22)$$

$$p = \frac{T}{\pi^2 \hbar^3 t^q} \sum_{v=\text{hh, lh}} m_v^q \sum_i \mathcal{F}_0 \left(\eta_h - \frac{E_{v,i}^{\text{th}}}{T} \right),$$

$$E_{v,i}^{\text{th}} \simeq \frac{\hbar^2}{2m_v} \left(\frac{l\pi}{t^q} \right)^2, \quad (1.23)$$

where m_{hh}^a and m_{lh}^a are the heavy and light hole masses in the quantum well, respectively, which may differ from the values for a bulk semiconductor. In this way, we have been able to simplify expressions for various physical quantities when the temperature is also a variable in the system of equations.

The particle current at the abrupt hetero-interface is due to thermionic emission. The net electron current toward the outside of the quantum well at the interface is simulated as

$$j_e = \frac{\bar{m}_e \bar{T}^2}{2\pi^2 \hbar^3} \left[\exp\left(\eta_e^{\text{in}} - \frac{E_C^{\text{out}} - E_C^{\text{in}}}{T^{\text{in}}}\right) - \exp(\eta_e^{\text{out}}) \right],$$

$$\bar{m}_e = 2 / (1/m_e^{\text{in}} + 1/m_e^{\text{out}}), \quad \bar{T} = (T^{\text{in}} + T^{\text{out}}) / 2,$$

where m_e^{in} is the effective mass of electrons for the node at the quantum-well side (lower E_C), while m_e^{out} is that for the side of higher band edge E_C . Variables such as η_e^{in} , η_e^{out} , E_C^{in} , and E_C^{out} are all similarly defined. Also, the corresponding energy current should be simulated accordingly. That is,

$$S_e = (E_C^{\text{out}} + T^{\text{in}} + T^{\text{out}}) j_e$$

at the hetero-interface. The net hole current and hole energy current are similarly expressed, taking both the heavy and light holes into account. Previous simulations of heterostructure lasers [15]–[19] were based solely on the drift-diffusion model for the carrier transport. This model yielding over-estimated drift velocity at the abrupt hetero-interface is not only physically incorrect, but also prone to poor convergence if the electrostatic potential varies strongly around the abrupt hetero-interface with high injection currents.

1.4 Conditioning the Heat Flow Equation

In numerical simulations with finite floating-point precision, one needs to consider the degree of conditioning of the system of partial differential equations (in our case, (1.6)–(1.7)). Notice that j_e and j_h are multiplied by E_C and E_V in (1.19) and (1.20), respectively. The energies E_C and E_V have been cited with no reference level, since the

zero point of energy can be chosen freely as long as it is consistent throughout. Then E_C and E_V are determined by solving the Poisson equation, and the absolute values of these two quantities from (1.12) are usually much greater than T , the thermal energy. Therefore, the magnitude of the first terms in (1.19)–(1.20) is much greater than the remainder of the equations. As a consequence, the heat flow equation, (1.6), becomes approximately equal to a linear combination of the carrier continuity equations, (1.7), whenever the recombination terms or the lattice heat flux term is much smaller than $|E_C \mathbf{j}_e - E_V \mathbf{j}_h|$ at any portion of the device profile. This results in an ill-conditioned matrix problem after discretization on a finite-precision digital computer, and may be the main cause of the poor convergence in many heat flow simulation problems which do not include the second terms in (1.19)–(1.20), or are not properly conditioned. It is, therefore, of great importance to choose an appropriate energy reference for E_C and E_V . A reasonable strategy for this choice is to separate reference levels for the two band edges. The radiative recombination rate term cancels out by choosing $E_C^{\text{ref}} = (\overline{E_C} + \overline{E_V})/2 + \hbar\bar{\omega}/2$ and $E_V^{\text{ref}} = (\overline{E_C} + \overline{E_V})/2 - \hbar\bar{\omega}/2$ for the two reference levels E_C^{ref} and E_V^{ref} , where $\overline{E_C}$ and $\overline{E_V}$ are the average values of conduction and valence band edges, respectively. Then,

$$\begin{aligned}
& c_p \frac{\partial T}{\partial t} + \frac{\partial}{\partial t} \left\{ N'_C T^{\frac{3}{2}} \left[\frac{3}{2} T \mathcal{F}_{\frac{3}{2}}(\eta_e) + \left(E_C - E_o - \frac{\hbar\bar{\omega}}{2} \right) \mathcal{F}_{\frac{1}{2}}(\eta_e) \right] \right. \\
& \quad \left. - N'_V T^{\frac{3}{2}} \left[\frac{3}{2} T \mathcal{F}_{\frac{3}{2}}(\eta_h) + (E_V - E_o + \hbar\bar{\omega}/2) \mathcal{F}_{\frac{1}{2}}(\eta_h) \right] \right\} \\
& - \nabla \cdot \kappa \nabla T + \nabla \cdot \left[(E_C - E_o - \hbar\bar{\omega}/2) \mathbf{j}_e + \mathbf{S}_e^{\text{kin}} \right. \\
& \quad \left. + (-E_V + E_o - \hbar\bar{\omega}/2) \mathbf{j}_h - \mathbf{S}_h^{\text{kin}} \right] \\
& - \hbar\bar{\omega} (U^{\text{HSR}} + U^{\text{Aug}} + R^{\text{fc}}) = 0, \tag{1.24}
\end{aligned}$$

$$E_o = (\overline{E_C} + \overline{E_V})/2,$$

where E_o is a constant energy offset chosen as the average of E_C and E_V at the electrode nodes from the boundary condition. This form has been found to work well for strongly forward-biased devices with high carrier and doping densities.

We think that the above method will work for most cases. For high voltage devices, it may be necessary to solve the equations first without the energy flow equation and get the profiles of E_C and E_V , and then set up energy references which are all different for all discretized equations.

1.5 Discretization of Flux Equations

To discretize the system of partial differential equations arising from (1.6)–(1.7), we use the finite-difference method with the box discretization scheme [20] applied to rectangular meshes. A well-known method for this type of discretization problem with uniform temperature was first introduced by Scharfetter and Gummel [21]. This method has been extended for the nonisothermal cases with simplified expressions for the nonisothermal currents in [22]–[23]. Here we show the results for our expressions in (1.15)–(1.20) for the fluxes.

We first transform the expressions for the flux densities for electrons, (1.15) and (1.19) into

$$\mathbf{j}_e = -M_e \{ T \gamma_0(\eta_e) \nabla \mathcal{F}_0(\eta_e) + \mathcal{F}_0(\eta_e) [\nabla E_C + 2\gamma_1(\eta_e) \nabla T] \}, \quad (1.25)$$

$$\begin{aligned} \mathbf{S}_e^{\text{kin}} = & -2M_e T \{ T \gamma_1(\eta_e) \nabla \mathcal{F}_1(\eta_e) \\ & + \mathcal{F}_1(\eta_e) [\nabla E_C + 3\gamma_2(\eta_e) \nabla T] \}, \end{aligned} \quad (1.26)$$

$$\gamma_j(\eta) \equiv \mathcal{F}_j(\eta) / \mathcal{F}_{j-1}(\eta).$$

Note that all orders of $\gamma_j(\eta)$ become 1 for a nondegenerate carrier system. We assume here that the potential and temperature are almost linear in the interval between two nodes, i and $i+1$, located at positions $x = x_i$ and x_{i+1} , respectively. Then the discretized

form for the electron flux in the $+x$ direction is found to be

$$j_e|_{i+\frac{1}{2}} = \frac{M_e|_{i+\frac{1}{2}}}{x_{i+1} - x_i} [B_1(\Delta\Psi, \Theta) \mathcal{F}_0(\eta_e|_i) - B_1(-\Delta\Psi, \Theta) \mathcal{F}_0(\eta_e|_{i+1})], \quad (1.27)$$

$$S_e^{\text{kin}}|_{i+\frac{1}{2}} = 2 T_{i+\frac{1}{2}} \frac{M_e|_{i+\frac{1}{2}}}{x_{i+1} - x_i} [B(\Delta\Psi_2, \Theta_2) \mathcal{F}_1(\eta_e|_i) - B(-\Delta\Psi_2, \Theta_2) \mathcal{F}_1(\eta_e|_{i+1})], \quad (1.28)$$

$$B(\Delta\Psi_j, \Theta_j) = \Delta\Psi_j / [\exp(\Delta\Psi_j / \Theta_j) - 1],$$

$$\Delta\Psi_j = E_{Ci+1} - E_{Ci} + (j+1) \gamma_j(\bar{\eta}_e) (T_{i+1} - T_i),$$

$$\Theta_j = \gamma_{j-1}(\bar{\eta}_e) (T_{i+1} + T_i) / 2,$$

$$\bar{\eta}_e = (\eta_e|_i + \eta_e|_{i+1}) / 2.$$

Here, a function $B(\cdot)$ has been introduced by modifying the Bernoulli function $B(\xi) = \xi / (e^\xi - 1)$ to accommodate the temperature gradient and Fermi-Dirac statistics. It is possible to use $\mathcal{F}_0(\cdot)$ instead of $\mathcal{F}_1(\cdot)$ only if we replace $B(\Delta\Psi_2, \Theta_2)$ with $\gamma_1(\bar{\eta}_e) B(\Delta\Psi_2, \Theta_1)$. That is,

$$S_e^{\text{kin}}|_{i+\frac{1}{2}} = 2 T_{i+\frac{1}{2}} \frac{M_e|_{i+\frac{1}{2}}}{x_{i+1} - x_i} \gamma_1(\bar{\eta}_e) [B(\Delta\Psi_2, \Theta_1) \mathcal{F}_0(\eta_e|_i) - B(-\Delta\Psi_2, \Theta_1) \mathcal{F}_0(\eta_e|_{i+1})]. \quad (1.29)$$

This scheme is used in actual implementation of the algorithm.

For the other three directions, and also for the four components of hole flux and energy flux, one may obtain similar expressions. Note that a nonuniform band structure such as graded heterojunctions in compound semiconductor devices are all included in the basic variables, without introducing additional parameters, which was suggested in [24], for numerical simulation.

Inside the quantum well with the staircase-like density of states, although the basic assumption used to derive the linearized carrier transport equations in (1.15)–(1.20) is not valid, we assume that those equations are still approximately valid with the adaptation that

$$\mathcal{F}_0(\eta_e) \text{ and } \mathcal{F}_0(\eta_p) \text{ are replaced by } n/N_C \text{ and } p/N_V, \quad (1.30)$$

respectively, where $\{n, p\}$ are those of (1.22)–(1.23). In a quantum-well laser, the overall carrier transport is hardly affected by the accuracy of the transport model for the quantum-well regions.

1.6 Boundary Conditions for the Heat Flow Equation

Boundary conditions represent a more complex problem for the heat transfer equation than for the ordinary carrier transport equations. Here we consider only special cases. The simplest case is a boundary contacting an ideal heat sink. This results in a Dirichlet boundary condition. The next simplest case is the von Neumann condition with vanishing heat flux for the air-semiconductor boundaries. For this condition, one neglects the small amount of heat dissipated to the air. The realistic boundary condition at the electrode is more complicated. Suppose that the total amount of heat-flow out of an electrode is given. This then becomes a heat current boundary condition similar to the carrier current boundary condition for the carrier continuity equations.

A simple schematic band diagram showing the two quasi-Fermi levels for a semiconductor laser diode with a strong forward-bias is shown in Figure 1.1. Although most injected carriers recombine at the junction region, still many not-yet-recombined carriers reach the electrodes. This is represented by the two split quasi-Fermi levels throughout the device. At the anode, such electrons lose energy to the lattice heating the contact region, while holes gain energy cooling the same region.

One-dimensional analysis for the heat generated at the metal-semiconductor Schottky contact was done by Stratton [25]. Here we should consider both electrons and holes

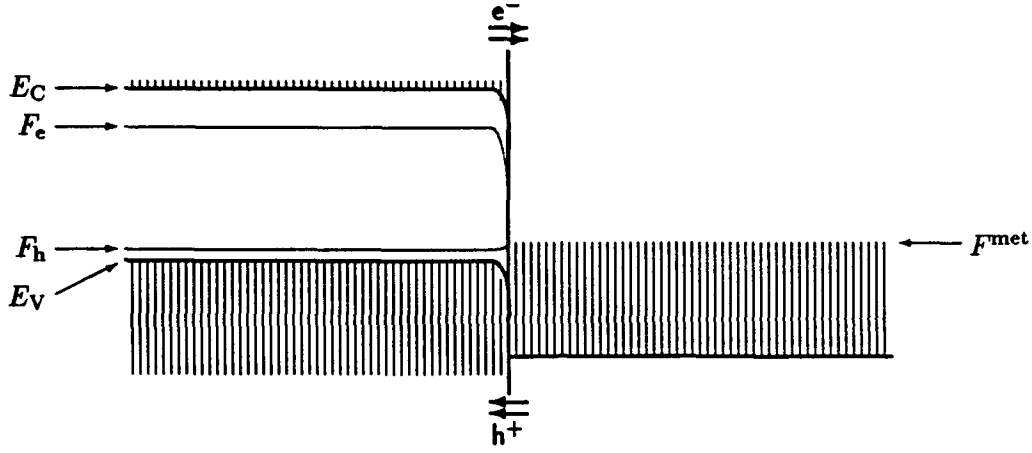


Figure 1.1: Schematic energy-band diagram for the quasi-Fermi levels in a forward-biased, one-dimensional, semiconductor laser diode.

together, and provide a two-dimensional formula permitting a variation of current along the contact. We assume that the contact is an ideal ohmic contact. The electrons or holes then meet either a tunneling barrier or a band discontinuity, and the incoming energy flux to the contact is described by

$$(\mathbf{S}_e - \mathbf{S}_h + \mathbf{S}_{\text{lat}} + \mathbf{S}_{\text{rad}}) \cdot \hat{\mathbf{n}}, \quad (1.31)$$

where $\hat{\mathbf{n}}$ is the outward normal unit vector at the contact. We only have a sea of electrons which are supported by an almost uniform Fermi level in the metal, F^{met} . Then the energy flux into the contact area is

$$(\mathbf{S}_e^{\text{met}} + \mathbf{S}_{\text{lat}}^{\text{met}}) \cdot (-\hat{\mathbf{n}}). \quad (1.32)$$

From the conservation of energy, the sum of (1.31) and (1.32) should be zero. Following [9], the energy flux carried by the electrons in the metal is $F^{\text{met}} + T\mathbf{J}_S^{\text{met}}$, where $\mathbf{J}_S^{\text{met}}$ is the entropy flux in the metal, and $T\mathbf{J}_S^{\text{met}}$ is sometimes called the “dissipative energy flux [26].” This last flux is again [13]

$$T\mathbf{J}_S^{\text{met}} = \pi^{\text{met}} \mathbf{j} - (K_e^{\text{met}} + \kappa^{\text{met}}) \nabla T, \quad (1.33)$$

where π^{met} is the Peltier potential [8]. The coefficients K_e^{met} and κ^{met} represent the electronic and lattice thermal conductivities, respectively, of the metal used for the electrode. The dissipative energy flow from the contact to the bulk metal region is

$$\int_{A_i^+} T \mathbf{J}_S^{\text{met}} \cdot \hat{\mathbf{n}} ds \equiv I_Q,$$

where integration is done over the area (in the metal side) of semiconductor-metal interface denoted by ' A_i^+ .' For the heat current boundary condition, we are to specify this quantity or provide necessary relations which specify this quantity at last. Then an equivalent expression provides the necessary boundary condition:

$$\int_{A_i^-} (\mathbf{S}_e - \mathbf{S}_h + \mathbf{S}_{\text{lat}} + \mathbf{S}_{\text{rad}}) \cdot \hat{\mathbf{n}} ds - \int_{A_i^+} F^{\text{met}} \mathbf{j} \cdot \hat{\mathbf{n}} ds = I_Q, \quad (1.34)$$

where $\int_{A_i^-}$ represents the area integration in the semiconductor side.

Note that an electron loses a considerable amount of energy when equilibrating at the contact, while a hole gains a slight amount. However, when the injection level is high, the number of holes injected at the anode can be so much larger than that of the electrons reaching the anode that the overall effect cannot be determined by calculating only the energy loss of electrons. Similar arguments can be applied to the cathode side. This time, electrons are cooling the contact region as a result.

By assuming an ohmic contact, the Fermi level of the metal can be seen as the equilibrium Fermi level of the semiconductor just inside the contact. Then the heat current boundary condition can be constructed as

$$\begin{aligned} \int_{A_i^-} [& (E_C^{\text{sem}} - F^{\text{eq}}) \mathbf{j}_e - (E_V^{\text{sem}} - F^{\text{eq}}) \mathbf{j}_h \\ & + \mathbf{S}_e^{\text{kin}} + \mathbf{S}_h^{\text{kin}} + \mathbf{S}_{\text{lat}}^{\text{sem}} + \mathbf{S}_{\text{rad}}] \cdot \hat{\mathbf{n}} ds = I_Q. \end{aligned} \quad (1.35)$$

We should express all the fluxes in the left-hand side in terms of chosen independent variables. With this expression for the heat current boundary condition, we can assign

a specific amount of heat flux for I_Q , or relate this expression with the formula which is to be obtained from physical consideration of the environment discussed in the next chapter.

Still not considered is the light absorption, denoted by \mathbf{S}_{rad} , at the electrode or the semiconductor-metal interface. In direct band-gap semiconductors with excess carriers, this contribution may not be ignored. For the stimulated emission in a semiconductor laser, the laser light does not hit the electrode metal directly. Although the metallic surface has a high reflectivity above 0.9, the tail of the Fabry-Perot mode pattern still intrudes into the metal to the skin depth, and the mode intensity is so great when lasing that we need to introduce a phenomenological radiation heat-coupling coefficient for each electrode. This absorption of light power is a part of the so-called waveguide loss, and thus the value of the coupling coefficient cannot be larger than what the waveguide loss coefficient implies. For the portions from the spontaneous emission and from the stimulated emission, we thus introduce respective power coupling coefficients χ_i^{sp} and χ_i^{st} as

$$\int_{A_i^-} \mathbf{S}_{\text{rad}} \cdot \hat{\mathbf{n}} ds = \int (\chi_i^{\text{sp}} E_g^+ U_{\text{rad}}^{\text{sp}} + \chi_i^{\text{st}} \hbar \omega U_{\text{rad}}^{\text{st}}) d^3 \mathbf{r}. \quad (1.36)$$

The right-hand side integration is carried out over the whole device volume. The values of these coefficients are considered to be strongly dependent on geometry.

CHAPTER 2

MINILASE AND TWO-DIMENSIONAL ANALYSIS OF QUANTUM-WELL LASERS

2.1 Introduction

Semiconductor lasers have mainly been analyzed by use of analytical or simple numerical models. Such models, however, cannot fully account for the multidimensional nature of light and carrier interactions in various laser structures. Even for a simple wide-stripe laser, the effects of laser switching, multimode behavior, and particularly the semiconductor quantum-well geometry can only be understood by elaborate numerical techniques. Two-dimensional simulators have previously been developed by other groups [15]–[19]. Of particular interest is the pioneering work of Wilt and Yariv [15]. Our simulator, “MINILASE,” represents an improvement for the design of quantum-well lasers and high-power semiconductor lasers. It can account for heat conduction, temperature distribution, and multiple spectral mode behavior as well as other two-dimensional characteristics of carrier flow and optical intensity profile.

The design goal of MINILASE is a correct implementation of semiconductor physics. Since it solves for the internal temperature distribution, it should be useful in long-wavelength semiconductor laser applications, where the threshold current exhibits a strong temperature dependence, as well as for power semiconductor laser applications. Additionally, the fact that MINILASE correctly simulates the switching response of the laser will be useful in applications such as short-range optical communications in optical integrated circuits as well as high-speed long-distance data communication.

MINILASE has been designed as follows: For the electronic part, it discretizes, by the finite-box-integration method [20], four partial differential equations including the heat flow equation. It solves the resulting nonlinear simultaneous equations by the full-Newton

method for both steady-state and transient responses. For the optical part, it solves the Helmholtz eigenvalue equation on a two-dimensional cross-sectional plane, so that MINILASE can accommodate various profiles of compound semiconductor compositions. From an outer iteration with the photon rate equation, MINILASE yields the individual photon numbers of multiple spectral modes, which permits spectral mode analysis of the optical transition rates in semiconductor lasers.

We have applied our simulator to GaAs-AlGaAs graded-index-separate-confinement-heterostructure buried-quantum-well (GRINSCH buried-QW) lasers [27]. The results are in good agreement with the available experimental data.

2.2 Physical Considerations

At least four equations are necessary to simulate semiconductor lasers; the Poisson equation for the potential, the two continuity equations of the form given in (1.7) for the carrier transport, and the Helmholtz eigenvalue equation for the optical field. We add the heat flow equation given in (1.6) to obtain the temperature distribution. We henceforth call the first three equations and the heat flow equation the electronic part equations. Then the partial differential equations for the electronic part are

$$-\nabla \cdot \epsilon \nabla \psi + q(n - p - N_D^+ + N_A^-) = 0, \quad (2.1)$$

$$dn/dt + \nabla \cdot \mathbf{j}_e + U_{\text{rad}}^{\text{st}} + U_{\text{rad}}^{\text{sp}} + U_{\text{HSR}} + U_{\text{Aug}} = 0, \quad (2.2)$$

$$dp/dt + \nabla \cdot \mathbf{j}_h + U_{\text{rad}}^{\text{st}} + U_{\text{rad}}^{\text{sp}} + U_{\text{HSR}} + U_{\text{Aug}} = 0, \quad (2.3)$$

$$du/dt - \nabla \cdot \kappa \nabla T + \nabla \cdot \mathbf{J}_E + \hbar\omega(U_{\text{rad}}^{\text{st}} - R_{\text{fc}}) + E_G^+ U_{\text{rad}}^{\text{sp}} = 0. \quad (2.4)$$

Here ϵ is the static permittivity of the material, and N_D^+ [N_A^-] is the density of ionized donor [acceptor] impurities.

By introducing only one temperature (for both the electron gas and the crystal lattice) and only one equation for the heat transfer, we have assumed that phonon scattering

leads quickly to a local equilibrium. This assumption is valid since our scale of transient analysis is in the order of 1 ns, while the momentum relaxation time is in the order of 1 ps.

The Helmholtz equation can be derived from the Maxwell equations by ignoring spatial derivatives of $\hat{\epsilon}_\omega$, the relative permittivity at optical frequency ω , as follows:

$$\left(\nabla^2 + \hat{\epsilon}_\omega \omega^2 / c^2 - \beta^2\right) \phi = 0, \quad (2.5)$$

where c is the light velocity in a vacuum, and ϕ and β are the optical field and its propagation constant, respectively. Here we solve the two-dimensional Helmholtz equation directly rather than employing the effective refractive index method [28]. By doing this the simulator can exactly analyze virtually any refractive index profile. It should be noted however that this equation totally neglects the vectorial nature of the electromagnetics problem. We then simply use the Dirichlet boundary condition at the natural boundary assuming that the field amplitude at the boundary is negligible. When the device profile is symmetric, we use the vanishing Neumann boundary condition along the line of symmetry, and solve the equation in a half domain for a symmetrically designed profile. We fix ω at the center frequency of stimulated emission, and solve (2.5) for the eigenvalues β^2 and the corresponding eigenfunctions ϕ . Then we get multiple transverse mode solutions. We cannot actually predict how those transverse modes will develop. There are also multiple longitudinal modes which form a beat pattern in space, making the density of carriers irregular along the longitudinal direction. In our simulation, we have assumed that all the characteristics are uniform along the optical axis either because such an irregular beat pattern is random so that the overall effect can be ignored, or because only one optical mode is dominant, as in well-designed quantum-well lasers. Even for a double-heterojunction laser, when the laser is shorter than 50 μm long, we need not consider such a problem since there is only one longitudinal mode actually lasing.

Outer iteration is done with the photon rate equation in (1.5), viz.,

$$dS_\nu/dt = G_\nu S_\nu + R_\nu^{sp} - S_\nu/\tau_\nu.$$

We have used a form which explicitly involves the mode occupation number S_ν of each mode ν . In principle, we can get a self-consistent solution if we solve the above six equations iteratively.

2.3 Modeling of physical Parameters

2.3.1 Sources of Poisson equation

Throughout the formulation, we intentionally use the variables η_e and η_h rather than carrier densities, n and p , which can be expressed in terms of the former variables as in (1.8). These expressions are valid in the regions whose band edges can be approximated to be parabolic. However, in size-quantized regions, i.e., inside the quantum well, we need to use (1.22)–(1.23) with $m_{hh}^q = 0.45m_0$ and $m_{lh}^q = 0.08m_0$ according to [29] for GaAs.

In the semiconductor laser application, we cannot ignore incomplete ionization of dopants. Specifically we use, for N_D^+ and N_A^- ,

$$N_D^+ = \frac{N_D}{1 + 2 \exp(\eta_e + \epsilon_D/T)}, \quad N_A^- = \frac{N_A}{1 + 4 \exp(\eta_h + \epsilon_A/T)}, \quad (2.6)$$

where ϵ_D and ϵ_A are the absolute values of the energy levels of donor and acceptor states, respectively, with respect to the corresponding band edges.

2.3.2 Hall-Shockley-Reed recombination

For the modeling of the Hall-Shockley-Reed (HSR) recombination rate, we use

$$U_{\text{HSR}} = \frac{np - n_0p_0}{\tau_e(n + n_1) + \tau_h(p + p_1)}, \quad (2.7)$$

$$n_0 = N'_C T^{3/2} \mathcal{F}_{1/2}(\bar{F} - E_C)/T,$$

$$p_0 = N'_V T^{3/2} \mathcal{F}_{1/2}(E_V - \bar{F})/T,$$

$$n_1 = N'_C T^{3/2} \mathcal{F}_{1/2}((E_T - E_C)/T),$$

$$p_1 = N'_V T^{3/2} \mathcal{F}_{1/2}((E_V - E_T)/T),$$

$$\bar{F} \equiv (F_e + F_h)/2$$

where n_0p_0 is the product of equilibrium densities of electrons and holes, while n_1 and p_1 are the respective densities when the Fermi energy is positioned at the trap energy level E_T . The HSR recombination is a typical nonradiative recombination, and this generates heat when the net effect is a recombination of electron-hole pairs. The strength of this is modeled by the parameters τ_n and τ_p in (2.7). The numerical values for this depends on the purity of the device and crystal defects. In the simulation example, we use $\tau_n \simeq \tau_p \simeq 5 \cdot 10^{-8}$ s throughout the whole device, assuming that the device is free of defects so that the HSR recombination is not a major recombination process. Obviously, the values for τ_n and τ_p can be changed locally if necessary.

2.3.3 Auger recombination

It is known that Auger recombination is not as crucial for the temperature dependence of the threshold current in GaAs-AlGaAs lasers as it is in long-wavelength lasers (e.g., InGaAsP lasers). There are several different kinds of Auger processes according to which bands are involved—CCCH, CHHS, and CHHL processes—and to whether the phonon is involved—phonon-less CHHS and phonon-assisted CHHS processes. For semiconductors with $E_G > \Delta$, the CHHL process is negligible compared to the CHHS process. For

GaAs, the Auger coefficient for phonon-less CCCH process is zero, since the condition of energy-momentum conservation is not satisfied [30], [31]. Among the various kinds of phonon-scattering which assist the Auger processes, the deformation-potential LO-phonon-scattering is known to be most responsible for Auger recombination at low temperatures, followed by the polar-optical LO-phonon-scattering [32], [33]. These two kinds of phonon-assisted Auger processes yield relatively weak temperature dependence. Consequently, we only have the LO-phonon-assisted CCCH process for C_n , whereas we have the phonon-less and the LO-phonon-assisted CHHS processes for C_h in the following model:

$$U^{\text{Aug}} = [C_p p + C_n^{\text{ph}} n^\Gamma] (n^\Gamma p - n_0^\Gamma p_0), \quad (2.8)$$

where n^Γ is the electron density in the Γ valley.

For $\text{Al}_x\text{Ga}_{1-x}\text{As}$, we take

$$C_p(x) = C_p(0) \left\{ [E_G^\Gamma(0) - \Delta(0)] / [E_G^\Gamma(x) - \Delta(x)] \right\}^{\gamma_A} \quad (2.9)$$

$$C_n(x) = C_n(0) [E_G(0)/E_G^\Gamma(x)]^{\gamma_A} \quad (2.10)$$

with $\gamma_A \simeq 1.5$ from approximate expressions in [31].

For the quantum-well active layer, the work of Takeshima [34] suggests that $C_n \ll C_p$ also for the quasi-two-dimensional gases. Since the quantum-well active layer is normally undoped, and has almost the same densities of electrons and holes, we thus can ignore the CCCH process. It was found that the phonon-assisted CHHS process for a quantum-well laser has only a weak temperature dependence [34]. The well-thickness dependence of Auger processes at room temperatures was also found to be weak around the threshold injection carrier densities of a quantum-well laser [35], [34]. Hence, for the GaAs quantum-well active layer, we use the room-temperature Auger coefficients of the bulk GaAs for all temperatures for C_p in the first approximation.

Table 2.1: GaAs Characteristics

parameters	symp.	data	ref.
Spontaneous recomb. coeff.	B_0	$0.77 \cdot 10^{-10} \text{ cm}^3/\text{s}$	[36]
CCCH Auger coeff. at 300 K	C_n	$10^{-36} \text{ cm}^6 \cdot \text{s}^{-1}$	[37]
Phonon-less CHHS Auger coeff. at 600 K	C_p^{s-ph}	$2 \cdot 10^{-29} \text{ cm}^6 \cdot \text{s}^{-1}$	[38]
Phonon-assisted CHHS Auger coeff. at 100 K	C_p^{ph}	$10^{-32} \text{ cm}^6 \cdot \text{s}^{-1}$	[39]
Energy band gap at 0 K	$E_G(0)$	1.519 eV	[40]
Energy bandgap temperature parameters	α_{E_G}	$5.405 \cdot 10^{-4} \text{ eV} \cdot \text{K}^{-1}$	[40]
	θ	204 K	[40]
Temper. coeff. for free electron absorption	γ_n^{fc}	0.34	[41]
LO phonon energy	$\hbar\omega_{\lambda}^{LO}$	29.6 meV	[39]
Threshold momentum parameter for CHHS Auger process	α	0.22	[31]
[100]-plane quantum-well eff. heavy hole mass	m_{hh}^q	$0.45m_0$	[29]
[100]-plane quantum-well eff. light hole mass	m_{lh}^q	$0.08m_0$	[29]
Electron mobility parameters for ionized-impurity scattering	N_e^{ion}	$9.85 \cdot 10^{16} \text{ cm}^{-3}$	[42]
	α_e^{ion}	0.553	[42]
Hole mobility at 300 K [$\text{cm}^2/\text{V} \cdot \text{s}$]	μ_h	400	[43]
Hole mobility param. for ionized-impurity scattering	N_h^{ion}	$6.25 \cdot 10^{17} \text{ cm}^{-3}$	[44]
Carrier-density dependence of refractive index	$\frac{dN}{d\sqrt{np}}$	$-1.05 \cdot 10^{-20} \text{ cm}^3$	[45]
Thermal coeff. of refractive index	β_T^N	$4.9 \cdot 10^{-4} \text{ K}^{-1}$	[46]
Free carrier absorption cross section	σ_n^{fc}	$3 \cdot 10^{-18} \text{ cm}^2$	[47]
	σ_p^{fc}	$7 \cdot 10^{-18} \text{ cm}^2$	[47]

The physical parameters used for the computation of Auger recombination for GaAs are shown in Table 2.1.

2.3.4 Radiative recombination

Above threshold, we have stimulated emission as well as spontaneous emission. Either type of light emission comes from both the heavy-hole ($v = e\text{-}hh$) and light-hole ($v = e\text{-}lh$) transitions. Under the assumption of strict k -selection, the mode gain and spontaneous

emission factor in (1.5) can be expressed as

$$\begin{Bmatrix} G_\nu \\ R_\nu^{\text{sp}} \end{Bmatrix} = \int_V \begin{Bmatrix} r_\nu^{\text{st}} \\ r_\nu^{\text{sp}} \end{Bmatrix} |\hat{\phi}_\nu|^2 d^3\mathbf{r}. \quad (2.11)$$

$$|\hat{\phi}_\nu|^2 \equiv |\phi_\nu|^2 / \int_V |\phi_\nu|^2 d^3\mathbf{r}.$$

$$\begin{Bmatrix} r_\nu^{\text{st}} \\ r_\nu^{\text{sp}} \end{Bmatrix} = B_\nu \sum_{v=\text{e-hh}, \text{e-lh}} g_v(E_{\nu,h}^c - E_{\nu,h}^v) \begin{Bmatrix} f(E_{\nu,v}^c) - f(E_{\nu,v}^v) \\ f(E_{\nu,v}^c) [1 - f(E_{\nu,h}^v)] \end{Bmatrix}, \quad (2.12)$$

$$B_\nu = \frac{\pi q^2}{m_0^2 \epsilon_0 \omega_\nu \mathcal{N}^2} \overline{|M_b|^2},$$

$$\overline{|M_b|^2} \simeq \frac{m_0^2 E_G^\Gamma}{12 m_e^\Gamma} \frac{1 + \Delta/E_G^\Gamma}{1 + 2\Delta/3E_G^\Gamma}, \quad (2.13)$$

where B_ν is the Einstein coefficient of optical transition for mode ν , and \mathcal{N} is the refractive index around $E = \hbar\omega_\nu$. Integration denoted by \int_V is done over the whole volume of the laser cavity. The function $f(E)$ is the probability of an electron state at energy E being occupied, and the constant $\overline{|M_b|^2}$ is the mean absolute square of the matrix element of the momentum (to the optical polarization direction) obtained with respect to the Bloch wavefunctions for the conduction band electron state and a randomly polarized valence band electron state both at $\mathbf{k} = 0$ [48] [49]. We normally use the Fermi-Dirac probability function for $f(\cdot)$ by assuming that the local equilibrium is always maintained. The function $g_v(E_{\nu,v}^c - E_{\nu,v}^v)$ (with $v = \text{e-hh}, \text{e-lh}$) is the reduced density of states for optical transition between two levels of energy— $E_{\nu,v}^c$ in the conduction band and $E_{\nu,v}^v$ in the valence band.

$$E_{\nu,\text{e-hh}}^c \equiv E_C^\Gamma + \frac{\hbar\omega_\nu - E_G^\Gamma}{1 + m_e^\Gamma/m_{\text{hh}}}, \quad E_{\nu,\text{e-hh}}^v \equiv E_V - \frac{\hbar\omega_\nu - E_G^\Gamma}{m_{\text{hh}}/m_e^\Gamma + 1}.$$

The energies $E_{\nu,\text{e-lh}}^c$ and $E_{\nu,\text{e-lh}}^v$ are similarly defined with m_{hh} replaced with m_{lh} in the above equations. We optionally use a staircase quasi-two-dimensional density of states

for the quantum-well layer [50] and a square-root density of states for the other regions.

$$g_v(E)dE = \begin{cases} \frac{2m_v^q}{\pi\hbar^2 t^q} N_v^q(E) dE, & \text{in quantum-well,} \\ \frac{2m_v}{\pi^2\hbar^3} \sqrt{2m_v(E - E_G^\Gamma)} dE, & \text{otherwise,} \end{cases} \quad (2.14)$$

$$N_v^q(E) \cong \text{Int}\left(\frac{t^q}{\pi\hbar} \sqrt{2m_v^q(E - E_G^\Gamma)}\right), \quad (2.15)$$

for $v = \text{e-hh, e-lh}$ with

$$m_{\text{e-hh}} \equiv (1/m_e^\Gamma + 1/m_{\text{hh}}^\Gamma)^{-1}, \quad m_{\text{e-lh}} \equiv (1/m_e^\Gamma + 1/m_{\text{lh}}^\Gamma)^{-1},$$

$$m_{\text{e-hh}}^q \equiv (1/m_e^\Gamma + 1/m_{\text{hh}}^q)^{-1}, \quad m_{\text{e-lh}}^q \equiv (1/m_e^\Gamma + 1/m_{\text{lh}}^q)^{-1},$$

where t^q is the thickness of the quantum-well layer. The effective masses m_{hh}^q and m_{lh}^q are the heavy and light hole masses, respectively, in the quantum-well layer parallel to the [100] plane. Function $\text{Int}(x)$ takes the maximum non-negative integer less than x .

Experimental results do not show strict \mathbf{k} -selection. The opposite end to this model is no \mathbf{k} -selection except the subband selection, whose gain coefficient spectrum shape was found to agree better with experiment than strict \mathbf{k} -selection in the case of quantum-well lasers [51]. However, no- \mathbf{k} -selection model introduces several fitting parameters which are multiplication factors for the momentum matrix elements [52], [51]. We use a relaxed \mathbf{k} -selection model based on recent publications [53], [54], which will need an elaborate verification in the future. To simplify the convolution integral which is not acceptable in this two-dimensional simulation, we use the following multiplication factor $\rho^{\text{relx}}(E)$ which is multiplied to the reduced-density of states in (2.14). That is, for the transition between the conduction and the heavy hole bands,

$$\rho^{\text{relx}}(E) = \frac{1}{2} \left[1 + \tanh\left(\frac{E - E_{\text{e,i}}^{\text{th}} - E_{\text{hh,i}}^{\text{th}}}{E_{\text{relx}}}\right) \right], \quad (2.16)$$

where E_{relx} is a parametric relaxation energy for our approximation. We have chosen $E_{\text{relx}} \simeq 5$ meV in order to fit the results of [53]. Note that this relaxation reduces the maximum gain coefficient substantially, which in turn increases the threshold current estimation. For $v = \text{e-lh}$ of light-hole transition, $E_{\text{hh},i}^{\text{th}}$, $E_{\text{V},i}^{\text{hh}}$, and m_{hh}^{a} are replaced by $E_{\text{lh},i}^{\text{th}}$, $E_{\text{V},i}^{\text{lh}}$, and m_{lh}^{a} , respectively.

We have also incorporated polarization-dependent gain coefficient change for quantum-well lasers according to [55]. Between the two orthogonal polarization modes of guided optical fields, the transverse electric (TE) mode is usually dominant either because of the reflectivity difference from cleaved facets without special coating [56] or because of the low chance of the gain spectrum over the first light hole band being the peak. We therefore confine the treatment to that of the TE mode transition. For the transition between the conduction and the heavy hole bands,

$$\rho^{\text{TE}}(E) = \frac{3}{4} \left(1 + \frac{E_{\text{e},i}^{\text{th}} + E_{\text{hh},i}^{\text{th}}}{E - E_{\text{G}}^{\text{r}}} \right). \quad (2.17)$$

This extra factor is then multiplied to the reduced density of states as well as $\rho^{\text{relx}}(E)$. For the transition between the conduction and the light hole bands,

$$\rho^{\text{TE}}(E) = \frac{3}{4} \left(2 - \frac{E_{\text{e},i}^{\text{th}} + E_{\text{lh},i}^{\text{th}}}{E - E_{\text{G}}^{\text{r}}} \right). \quad (2.18)$$

The temperature dependence of the energy band gap of the active region material is of importance since the band gap determines the wavelength of the stimulated emission. We take Varshni's [57] formula:

$$E_{\text{G}}(T) = E_{\text{G}}(0 \text{ K}) - \alpha_{E_{\text{G}}} T^2 / (T + \theta). \quad (2.19)$$

The radiative recombination rate can also be represented in terms of r_{ν}^{st} and r_{ν}^{sp} as

$$U_{\text{rad}} = \sum_{\nu} r_{\nu}^{\text{st}} S_{\nu} |\hat{\phi}_{\nu}|^2 + \int \frac{\mathcal{N}^2 \mathcal{N}_{\text{g}} \omega^2}{\pi^2 c^3} r_{\nu}^{\text{sp}} d\omega, \quad (2.20)$$

The experimental data for the spontaneous radiative recombination factor $B_{\text{rad}}^{\text{sp}}(x)$ are not available for $\text{Al}_x\text{Ga}_{1-x}\text{As}$. However, we can deduce that it has only a small variation which comes from the functional dependence of the Einstein A coefficient. That is,

$$B_{\text{rad}}^{\text{sp}}(x) = B_{\text{rad}}^{\text{sp}}(0) \left[E_{\text{G}}(x) \overline{|M_{\text{b}}(x)|^2} / E_{\text{G}}^{\Gamma}(0) \overline{|M_{\text{b}}(0)|^2} \right], \quad (2.21)$$

where $\overline{|M_{\text{b}}(x)|^2}$ is given in (2.13) with x -dependent m_{e}^{Γ} and E_{G}^{Γ} .

The numerical integration in (2.20) imposes a heavy computational load. We therefore compute the second term of the right-hand side of (2.20) with (2.12) inside the active layer only, where most radiative recombination takes place. In the other regions, we approximate (2.20) into

$$U_{\text{rad}} = \sum_{\nu} r_{\nu}^{\text{st}} S_{\nu} |\dot{\phi}_{\nu}|^2 + B_0 (n^{\Gamma} p - n_0^{\Gamma} p_0).$$

The value of the constant B_0 is given in Table 2.1.

2.3.5 Refractive index

To accommodate the refractive index variations for all the regions including the active layer, we use the following formula:

$$\hat{\epsilon}_{\omega} = \left[\mathcal{N}_0 + \left(\frac{d\mathcal{N}}{d\sqrt{np}} \right)_{T=T_0}^{\text{b-t-b}} \sqrt{np} + \beta_T^{\mathcal{N}} (T - T_0) \right]^2 + \Delta\hat{\epsilon}_{\omega}^{\text{fc}}, \quad (2.22)$$

$$\Delta\hat{\epsilon}_{\omega}^{\text{fc}} = -\frac{q^2}{\epsilon_0 \omega^2} \left(\frac{n^{\Gamma}}{m_{\text{e}}^{\Gamma}} + \frac{n^{\text{X}}}{m_{\text{e}}^{\text{X}}} + \frac{n^{\text{L}}}{m_{\text{e}}^{\text{L}}} + \frac{p}{m_{\text{h}}} \right),$$

where ϵ_0 is the vacuum permittivity, $\beta_T^{\mathcal{N}}$ is the thermal coefficient of refractive index change, and $\left(d\mathcal{N}/d\sqrt{np} \right)_{T=T_0}^{\text{b-t-b}}$ represents the change due to band-to-band transitions of carriers via the Kramers-Krönig relation. The latter value for the active region is obtained by subtracting the theoretical free-carrier components from the empirical data of [45] for the overall carrier-density dependence. In (2.22), \sqrt{np} has been taken to interpret the empirical values obtained under the approximation $n \simeq p$ in the active layer. For the

other regions, we neglect the change in (2.22) due to the band-to-band transition, either because the absorption edge is well above the stimulated emission frequency or because the optical field intensity is negligibly small in those regions.

For strongly gain-guided structures, we should include change of the imaginary part of the refractive index. This results in a complex matrix of a non-Hermitian type after discretizing the Helmholtz equation, (2.5). The work for the gain-guided structures is reserved for future research.

2.3.6 Free-Carrier absorption and photon lifetime

The free-carrier absorption rate is proportional to the light intensity and the carrier densities. It is related to the free-carrier-absorption coefficient α^{fc} , evaluated for a bulk semiconductor, as follows:

$$R^{fc} = \frac{c}{\mathcal{N}_g} \alpha^{fc} \sum_{\nu} S_{\nu} |\hat{\phi}_{\nu}|^2, \quad \alpha^{fc} = \sigma_n^{fc} n + \sigma_p^{fc} p,$$

where σ_n^{fc} and σ_p^{fc} is the free-carrier-absorption cross-sections for electrons and holes, respectively. The temperature variation of these coefficients for bulk GaAs is not strong. For instance, in the case of electrons, we can only deduce $\tau_e^{fc} \sim T^{0.3}$ around 300 K from the data in [41]. We therefore ignore temperature dependence of the free-carrier-absorption coefficients, and take a simple model [47] of constant σ_n^{fc} and σ_p^{fc} .

For the graded-junction cladding layers which sandwich the active layer, to our knowledge, experimental data are not yet available for the various mole fraction x of AlAs. We thus proceed with approximate values deduced from the available GaAs data.

The overall free-carrier-absorption coefficient for the calculation of photon lifetime τ_{ν} follows from the above absorption rate as

$$\alpha_{\nu}^{fc} = \int_V \alpha^{fc} |\hat{\phi}_{\nu}|^2 d^3\mathbf{r}. \quad (2.23)$$

The overall inverse photon lifetime which we need for (1.5) is then expressed as

$$\tau_{\nu}^{-1} = v_g \left[\alpha_{\nu}^{\text{fc}} + \alpha_{\nu}^{\text{w-g}} + (2L)^{-1} \ln(1/R_1 R_2) \right], \quad (2.24)$$

where v_g is the group velocity of mode ν , and $\alpha_{\nu}^{\text{w-g}}$ is the waveguide-scattering loss coefficient for mode ν , which depends on geometrical irregularity formed during the fabrication process of the laser waveguide.

Since there are graded heterojunction regions in the profile of semiconductor lasers, we need values of material parameters as functions of variable Al composition. In Table 2.2, such parameters which are obtained with a linear or quadratic interpolation are shown. In the table the lattice thermal conductivity κ in (2.4) is represented by the inverse, whose quadratic approximation fits better with experiments than that of κ itself. However, parameters such as carrier mobilities are not as simple to be represented as others in Table 2.2.

2.3.7 Carrier mobilities of $\text{Al}_x\text{Ga}_{1-x}\text{As}$

The electron mobility reflects the lowest band minimum among three conduction band minima, Γ , L , and X . We seek to express the experimental results in [68] as follows:

$$\mu_e^{\text{n-deg}} = \begin{cases} 8000 - 1.818 \cdot 10^4 x, & 0 < x < 0.429, \\ 90 + 1.145 \cdot 10^5 (x - 0.46)^2, & 0.429 \leq x < 0.46, \\ 90 + 3.75 \cdot 10^4 (x - 0.46)^2, & 0.46 \leq x < 0.50, \\ 200 - 2.0/(x - 0.46), & 0.50 \leq x \leq 1, \end{cases} \quad (2.25)$$

in units of $\text{cm}^2/\text{V}\cdot\text{s}$. The temperature dependence of electron mobility in doped AlGaAs (or even GaAs) is not well modeled due to various factors including the above-mentioned complex conduction band structure [63]. The modeling of this is reserved for future work.

scattering-limited Here we multiply a crude doping-dependence factor to the expression for the electron mobility of lightly doped AlGaAs in (2.25). This factor was taken

Table 2.2: $\text{Al}_x\text{Ga}_{1-x}\text{As}$ Characteristics

parameters	symp.	function of x , Al composition	ref.
Static permittivity	$\hat{\epsilon}$	$13.18 + (10.06 - 13.18) x$	[58],[59]
Refractive index at $\hbar\omega_{\nu} = 1.38$ eV	\mathcal{N}	$3.590 - 0.710x + 0.091x^2$	[47]
High freq. permittivity	$\hat{\epsilon}_{\infty}$	$10.89 + (8.16 - 10.89) x$	[58],[59]
Γ valley energy gap at 300 K [eV]	E_{G}^{Γ}	$1.424 + (2.671 - 1.424) x$	[47]
and its temper. change [eV/K]	$\frac{dE_{\text{G}}^{\Gamma}}{dT}$	$[-3.95 - (5.1 - 3.95) x] \cdot 10^{-4}$	[60],[61]
X valley energy gap at 300 K [eV]	E_{G}^X	$1.9 + (2.168 - 1.9) x$	[62],[63]
and its temper. change [eV/K]	$\frac{dE_{\text{G}}^X}{dT}$	$-3.6 \cdot 10^{-4}$	[61],[63]
Diff. between the valence band and spin-split band edges [eV]	Δ	$.340 - .040x$	[63]
Donor ionization energy for Γ band [meV]	ϵ_{Γ}	$5 + 5x$	[64],[63]
Donor ionization energy for X band [meV]	ϵ_X	$25 + 10x$	[64],[63]
LO phonon energy [meV]	$\hbar\omega_{\lambda}^{\text{LO}}$	$36.25 - 6.55x + 1.79x^2$	[65]
Γ valley electron mass	m_{e}^{Γ}	$.067 + (.15 - .067) x [m_0]$	[47]
X valley density-of-states-equiv. electron mass	m_{e}^X	$.32 + (.26 - .32) x [m_0]$	[63]
Heavy hole mass	m_{hh}	$.62 + (.76 - .62) x [m_0]$	[66]
Light hole mass	m_{lh}	$.087 + (.15 - .087) x [m_0]$	[66],[67]
Thermal resistivity [K·cm/W]	W	$2.27 + 28.83x - 30x^2$	[63]

from data in [42] for GaAs.

$$M_e = (\mu_e^{\text{n-deg}} N_C)_{T=T_0} \left[0.34 + \frac{0.66}{1 + \left(\frac{N_D^+ + N_A^- + p_{\text{hh}}}{N_e^{\text{ion}}} \right)^{\alpha_e^{\text{ion}}}} \right]. \quad (2.26)$$

where p_{hh} is the density of heavy holes which act like ionized impurities for electrons [69].

To our knowledge, no experimental data published for the compositional variation of the hole mobility in $\text{Al}_x\text{Ga}_{1-x}\text{As}$ are available. We generalize the theoretical scheme in [70] for the mobility parameter M_h as

$$\begin{aligned} \frac{1}{M_h} = \frac{1}{\left[\mu_h^{\text{n-deg}} N_V \right]_{x=0}} & \left[\frac{1/\epsilon_s(x) - 1/\epsilon_\infty(x)}{1/\epsilon_s(0) - 1/\epsilon_\infty(0)} \left(\frac{T}{T_0} \right)^{0.8} \right. \\ & \left. + \frac{N_D^+ + N_A^-}{N_h^{\text{ion}}(0)} \frac{m_{\text{hh}}(x) + m_{\text{lh}}(x)}{m_{\text{hh}}(0) + m_{\text{lh}}(0)} \left(\frac{\epsilon_{\text{st}}(0)}{\epsilon_{\text{st}}(x)} \right)^2 \left(\frac{T_0}{T} \right)^3 \right]. \end{aligned} \quad (2.27)$$

where N_h^{ion} refers to the parameter for the ionized-impurity-scattering-limited hole mobility for GaAs, and $m_{\text{hh}}(x)$ and $m_{\text{lh}}(x)$ represent the appropriate effective masses with the Al composition x . ϵ_∞ is the dielectric constant at high frequency, whose normalized value is found in Table 2.2.

2.4 Numerical Approach

The box-discretization [20] of these device equations has been used with the generalized Scharfetter-Gummel discretization scheme [21] described in Sec. 1.5. The four equations (2.1)–(2.4) for the electronic part are then solved by the full-Newton method and a sparse matrix package [71]–[72]. Since the current flow near the surface does not count for the overall characteristics in the case of semiconductor lasers, simple ohmic contacts at the electrodes have been assumed, and Neumann boundary conditions with

vanishing flux have been used at the surfaces without electrode contact throughout the simulation. Current boundary conditions and the heat current boundary conditions have been employed in consideration of application practice in driver circuits for semiconductor lasers.

The steady-state solution can be obtained by solving the steady-state problem for the electronic part equations by letting d/dt zero and solving the time-dependent problem for the rate equation. Other authors of semiconductor laser simulations used a simpler method which was described in [16]. However, when there are multiple modes competing with each other, such methods cannot be used.

Since we have adopted the full-Newton method to solve the electronic part equations, we can employ the fully-implicit-backward Euler method [14] to obtain the dynamic solver, thus avoiding the stability problem associated with the first-order time derivatives. The rate equation is also treated with the full-backward Euler method, and this rate equation is coupled with the electronic part equation by solving the two time dependent problems alternatively. The optical field pattern is obtained by solving the Helmholtz eigenvalue equation at each iteration. We should understand that the whole procedure of time dependent solution then does not become a fully implicit backward-Euler procedure since we still have two parts to be solved iteratively. This limits the size of the time step which is set especially during the transients of the relaxation oscillation which appears when the laser is driven by a step current.

The Helmholtz eigenvalue equation, (2.5), is solved by Rutishauser's subspace iteration subroutine RITZIT [73]. The routine solves for the desired number of eigenvalues of the largest magnitude and the corresponding eigenvectors. From the mathematical nature of the problem, the largest magnitude eigenvalues are negative. Therefore, we need to shift the spectrum to make the most positive eigenvalue—the fundamental transverse mode eigenvalue—the dominant one [74]. We then need not employ the inverse iteration. This method allows us to obtain only the desired physical eigenvalues and their characteristic optical field patterns.

The overall flowchart of the program is shown in Figure 2.1. It has an input card parsing structure. Graphical outputs are generated exclusively in the POSTSCRIPT language source code format, which allows a flexible, device-independent, and unilateral operation for all types of graphical output.

2.5 Application to Quantum-Well Lasers

We have applied our simulator to a 380 μm -long GaAs-AlGaAs GRINSCH buried-quantum-well laser [27], whose cross-sectional view is shown in Figure 2.2. The semiconductor equations yield the three solutions for the potential, the electron and the hole densities. The temperature distribution over the cross-sectional profile is depicted in Figure 2.3. We have assumed that the cathode is in contact with an ideal heat sink, and that the energy flow out of the anode side is negligible. We have found that electrons and holes are very effective energy carriers. The increase of the temperature slope in the middle of the cross section represents the poor thermal conductivity of AlGaAs compared to pure GaAs in the substrate. The hump above the quantum-well active region represents a heat dissipation from the electron system by the free-carrier absorption of the photon energy. The temperature elevation around the active layer depends strongly on the distance between the active layer and the heat sink.

The current flow diagram is shown in Figure 2.4. The figure shows that the reverse-biased junction across the blocking region of higher bandgap sufficiently channels the current through the narrow forward-biased region without introducing any insulator material into the laser profile. The thermionic injection current simulation has been found indispensable in the simulation of a quantum-well laser, since the different treatment of normalized carriers in the discretized carrier transport equations as described in (1.30) in the different regions of the device—inside and outside the quantum well—yields an unphysical result with only a drift-diffusion model applied everywhere. Figure 2.5 demonstrates this by showing the two uninterpolated pictures of current flow diagrams,

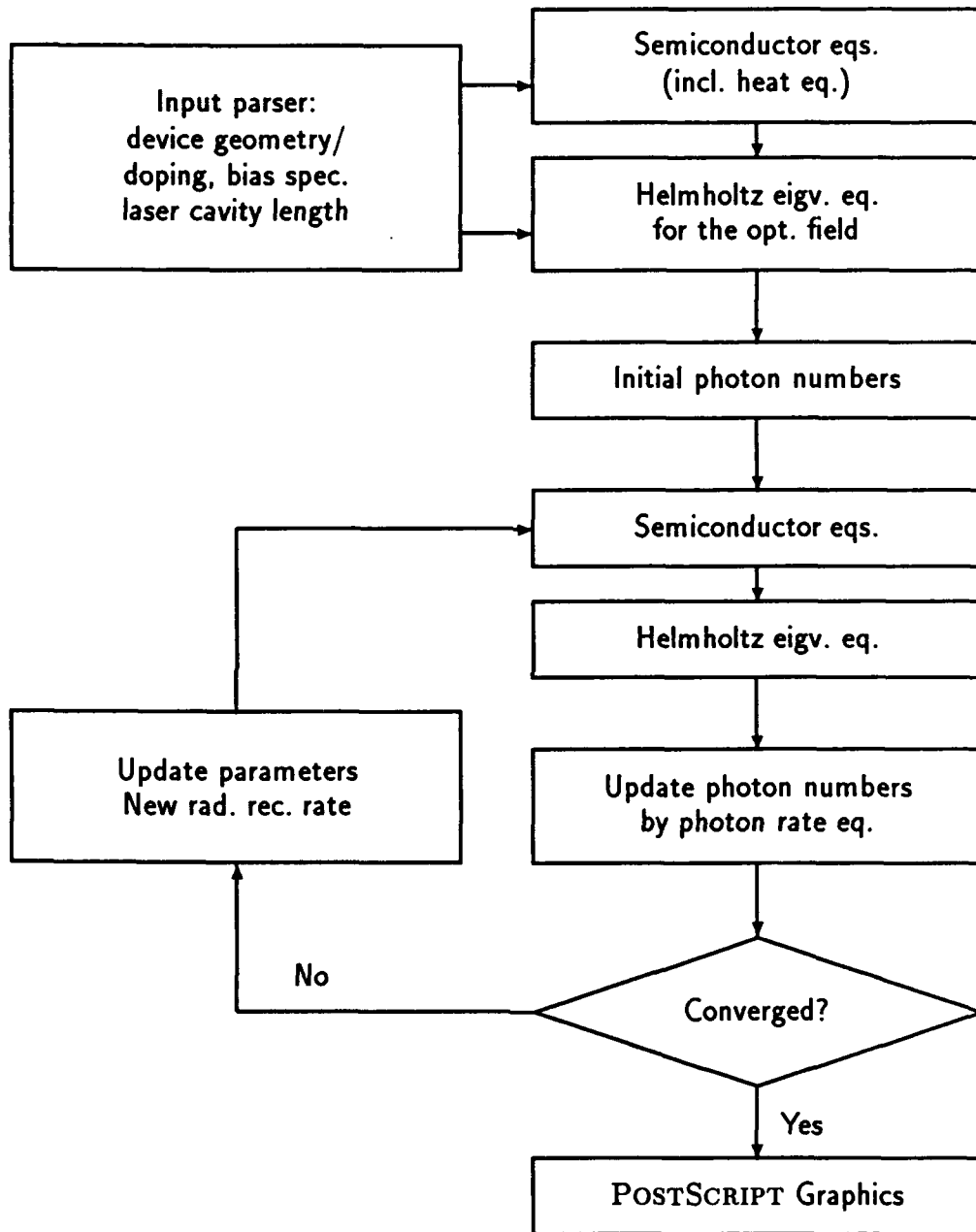


Figure 2.1: Flowchart of MINILASE.

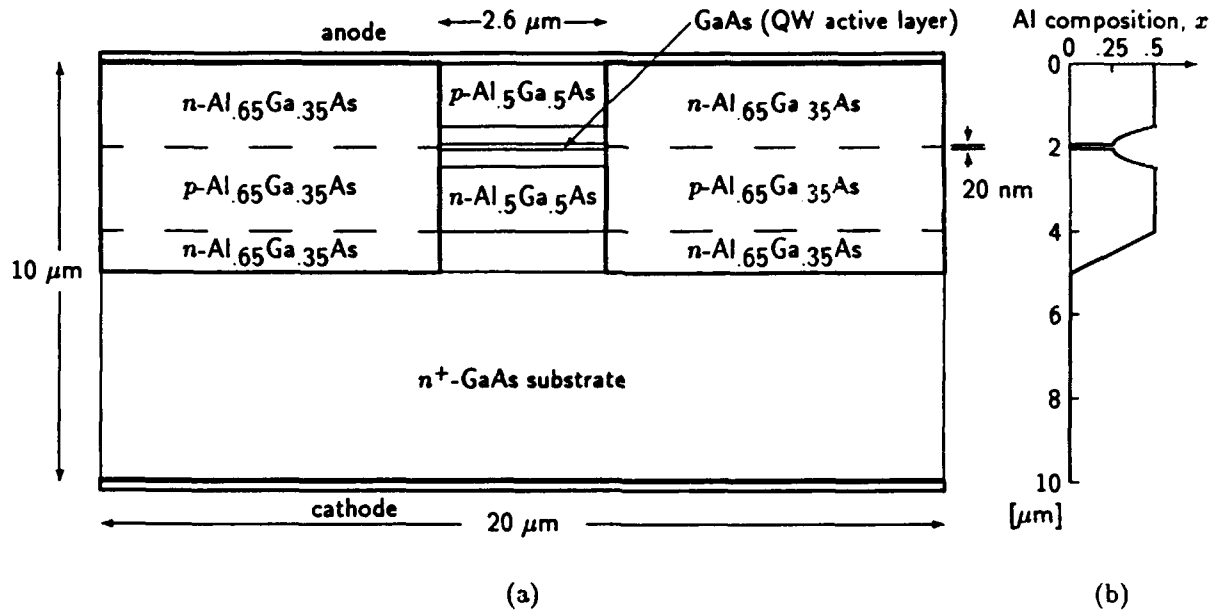


Figure 2.2: (a) Schematic cross-section of a simplified GaAs-AlGaAs graded-index-separate-confinement-heterojunction buried-quantum-well laser. The layers above and below the active layer are quadratically graded from $\text{Al}_{0.25}\text{Ga}_{0.75}\text{As}$ to $\text{Al}_{0.5}\text{Ga}_{0.5}\text{As}$. These three layers are undoped. (b) Variation of Al composition along the center line.

one with a thermionic emission simulation and the other with a drift-diffusion model only.

We have also obtained a light-current curve as shown in Figure 2.6 by varying the carrier injection. This shows a threshold current of $\sim 3.75\ \text{mA}$ and a local threshold current density of $380\ \text{A}/\text{cm}^2$ inside the channel between the two blocking regions of the higher bandgap. The latter number matches very well with various experimental data of broad-area single-quantum-well GRINSCH lasers [75]–[76]. The values from others' theoretical calculations [77], [50] vary from $240\ \text{A}/\text{cm}^2$ to $\sim 550\ \text{A}/\text{cm}^2$, since each author used different values for the material constants (*e.g.*, m_{hh}^q), the waveguide scattering loss coefficient, and the intrinsic loss coefficient, and also treated the k -selection rule and polarization dependence differently.

From the eigenvalue solver, we have obtained the optical field profile as shown in Figure 2.7. From the spectral analysis, we have obtained the gain spectra (Figure 2.8) and the optical output spectra (Figure 2.10) for various carrier injection levels. The

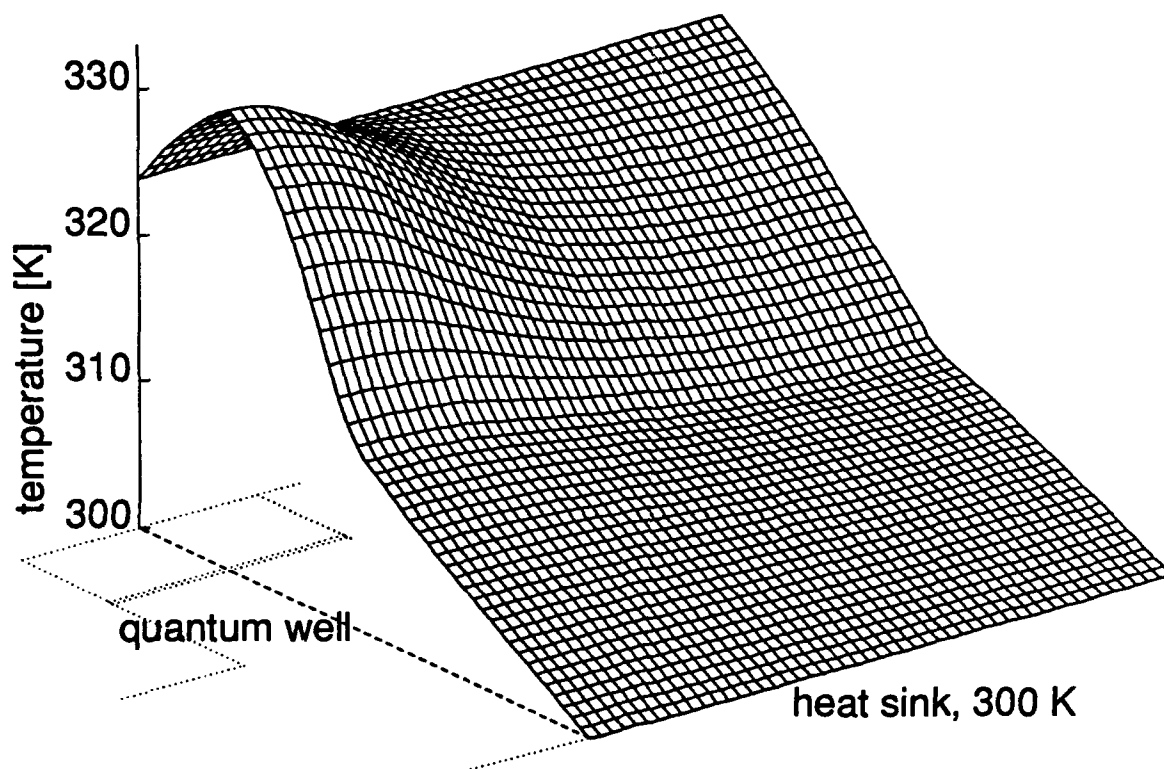


Figure 2.3: Temperature distribution profile for the half domain at a 180 mA current level. The cathode is assumed to be in contact with an ideal heat sink. Energy flow out of the anode side is assumed to be negligible.

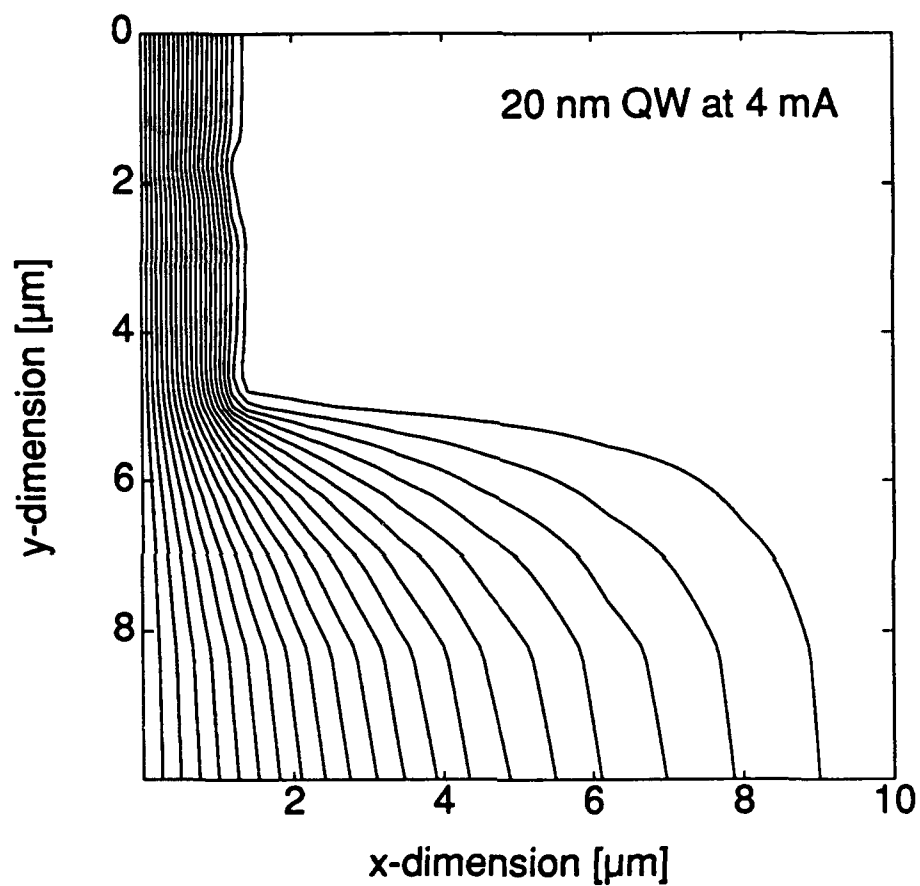
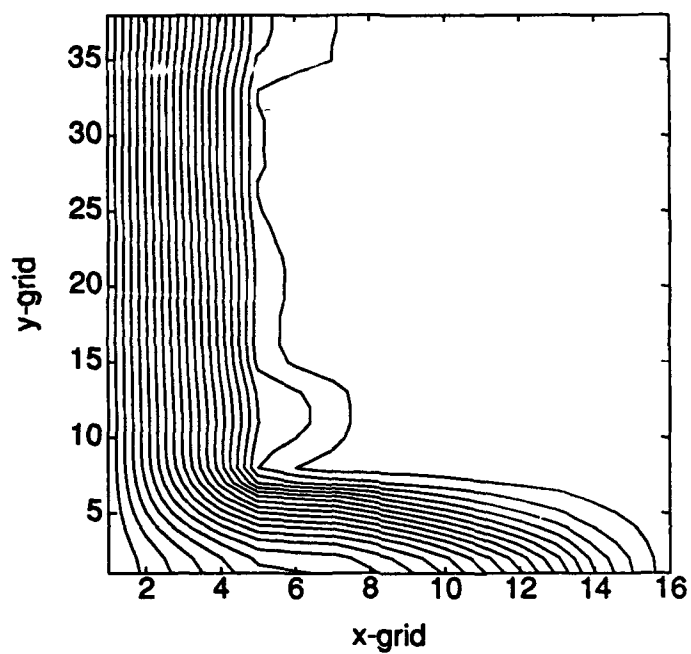
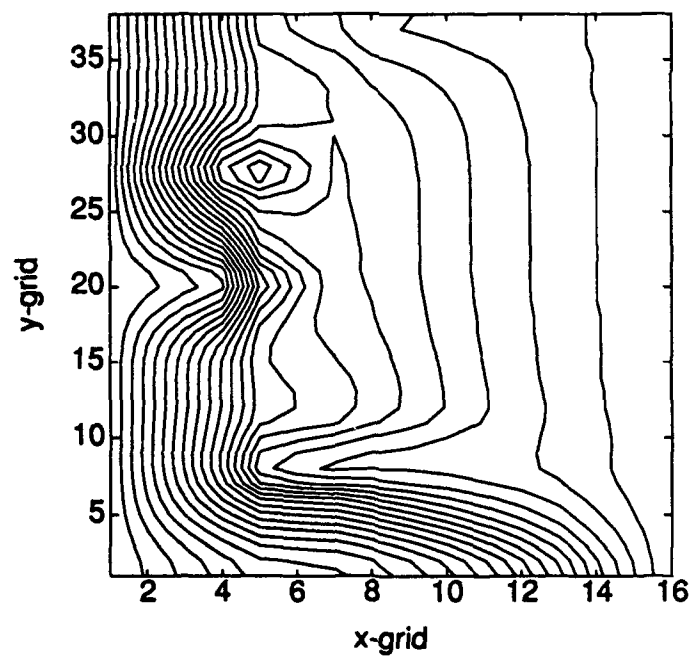


Figure 2.4: Current flow diagram for the half domain at 4.0 mA. One fortieth of the total current (electron current plus hole current) flows between the two adjacent lines in the diagram.

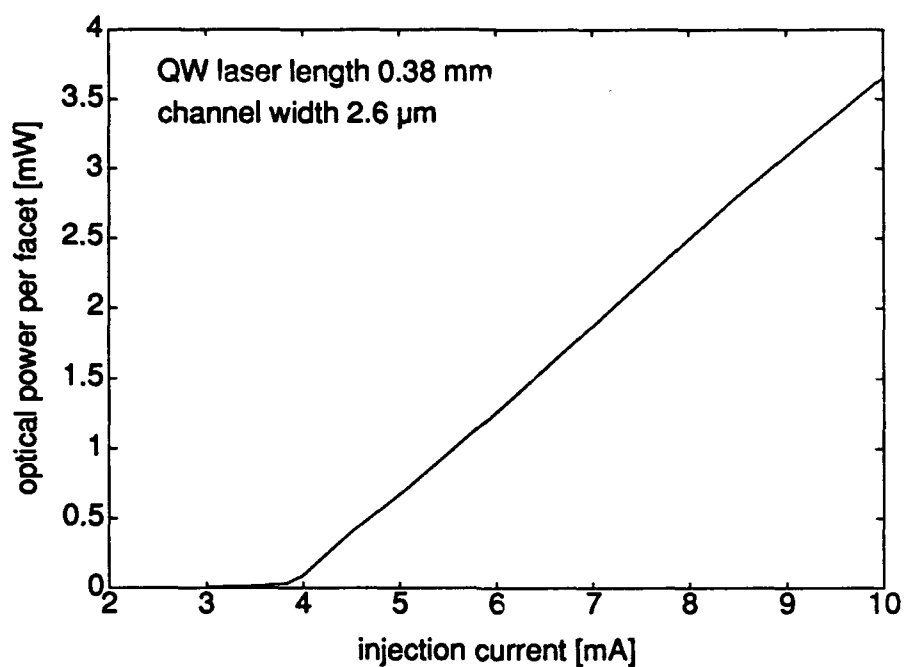


(a)

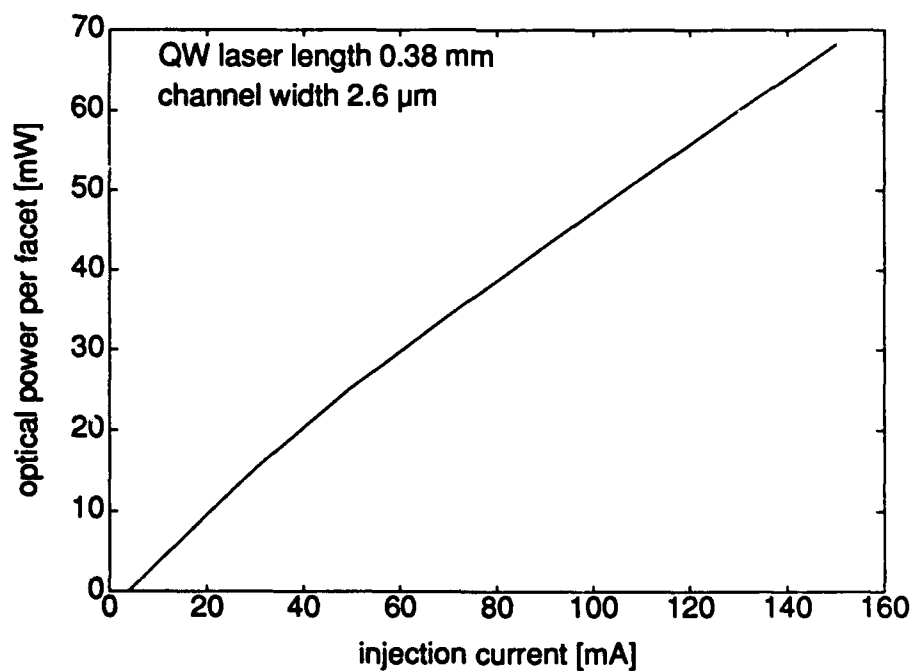


(b)

Figure 2.5: Uninterpolated current flow diagram for the half domain at 3 mA with simulations (a) of thermionic emission as well as drift-diffusion and (b) of drift-diffusion only.



(a)



(b)

Figure 2.6: Light-current curve of a model quantum-well laser. (a) Around the threshold. (b) Over the injection current of 0–160 mA.

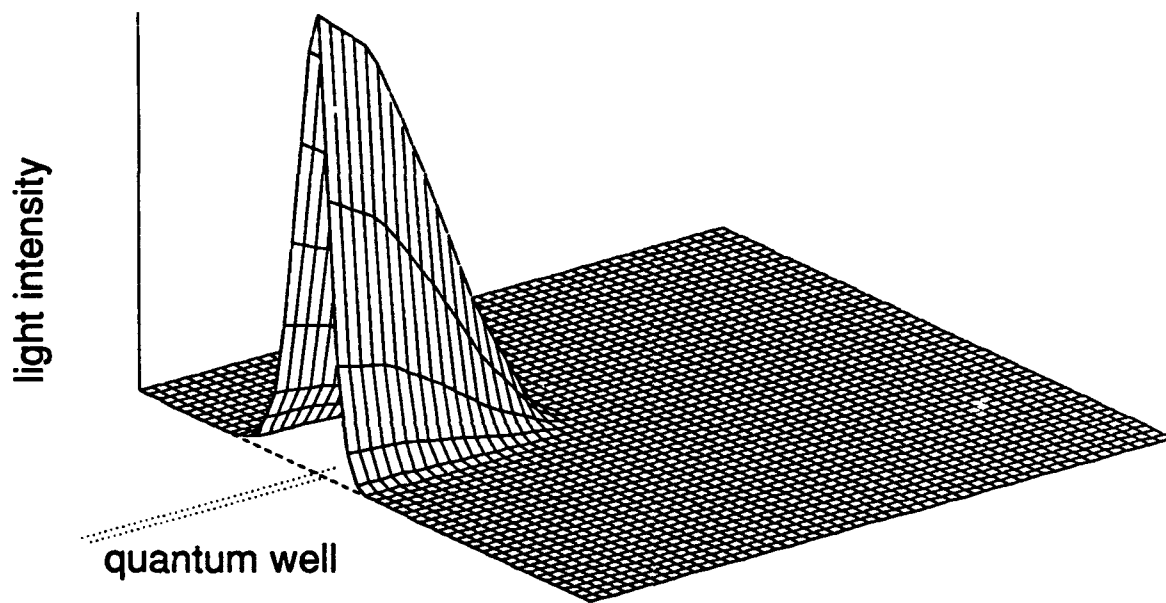
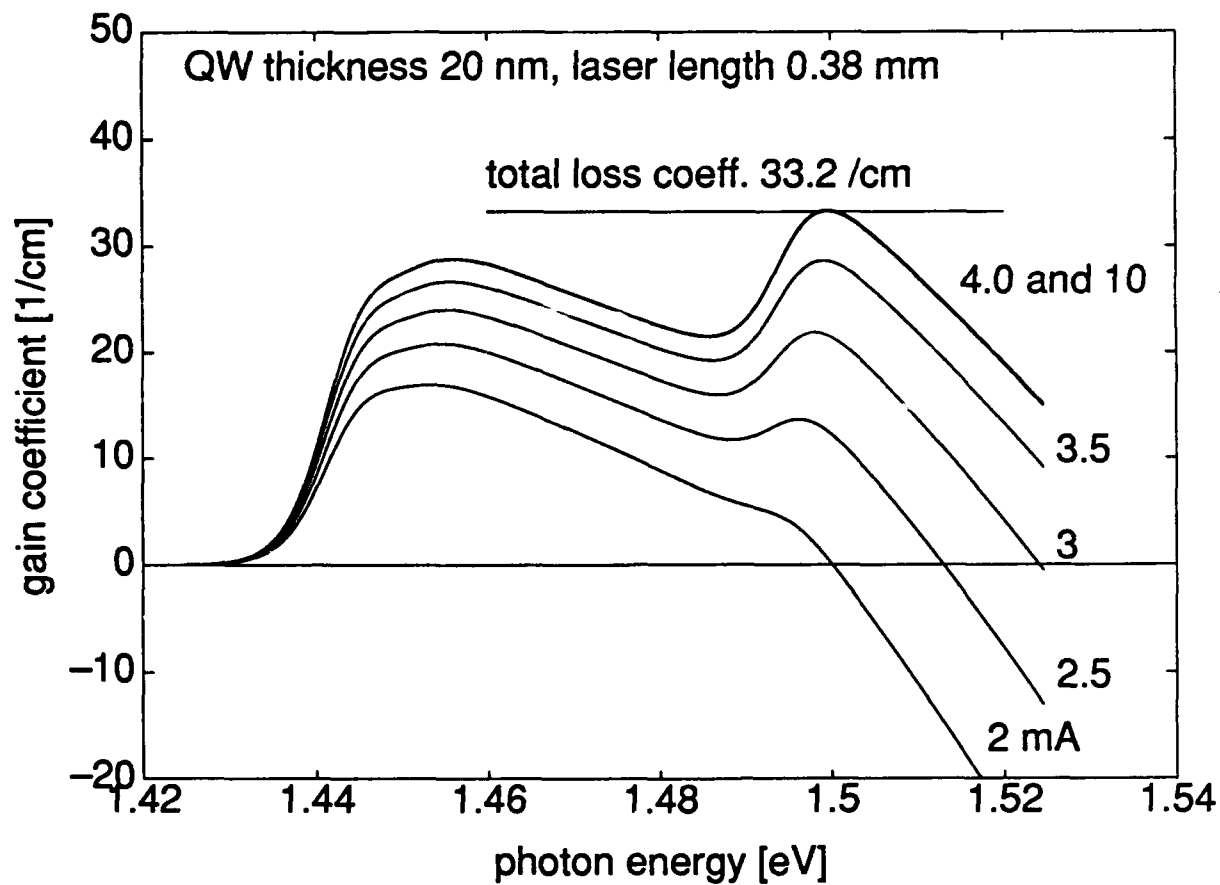


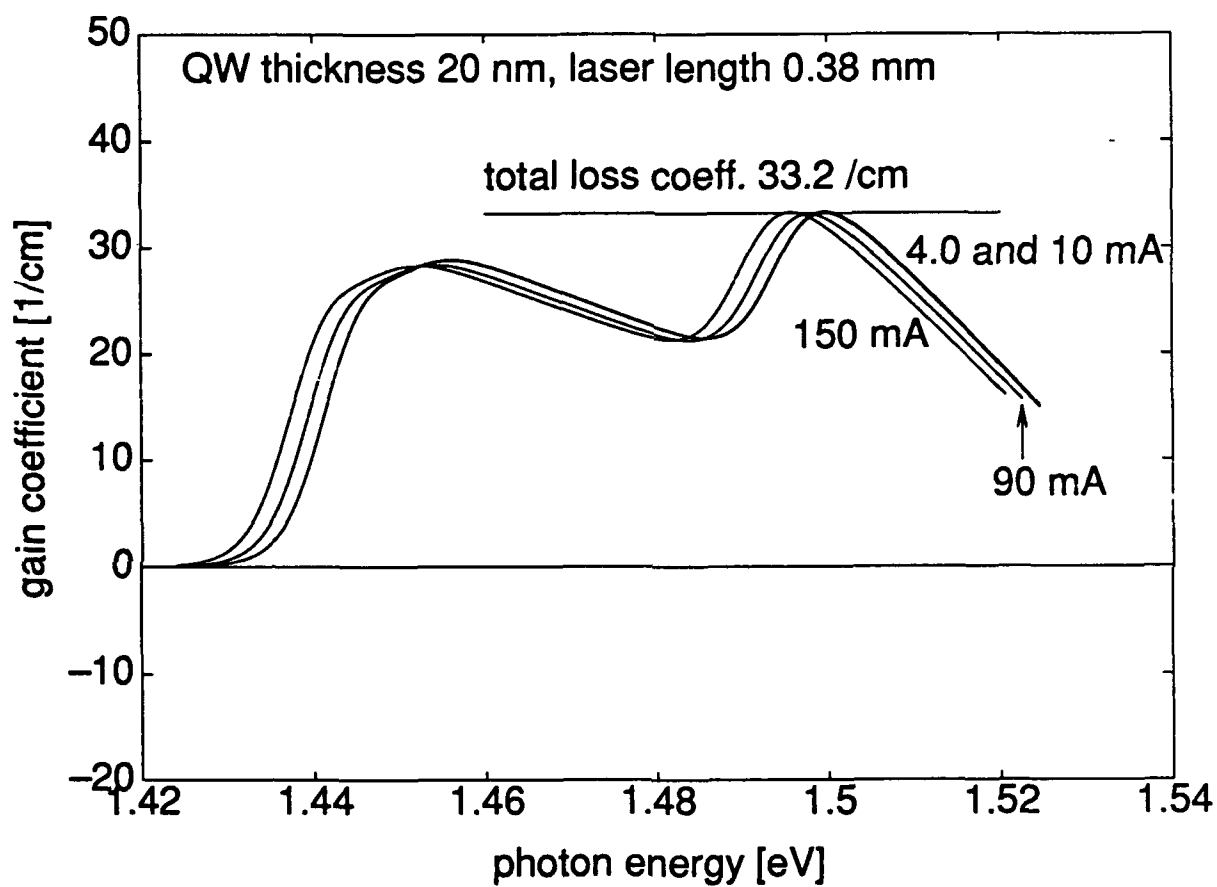
Figure 2.7: Optical intensity profile around the quantum-well region yielding an optical confinement factor of 3.9 %.



(a)

Figure 2.8: Gain coefficients at various current levels. Free-carrier loss has been obtained to be 2.0 /cm, and the waveguide scattering loss has been set at 5.0 /cm. (a) Around threshold level. The results show the gain saturation above the threshold.

(continued on p. 41)



(b)

Figure 2.8: (continued) (b) Far above threshold. The gain curve shifts to the lower energy spectrum as the current increases, because the band gap changes due to increasing temperature.

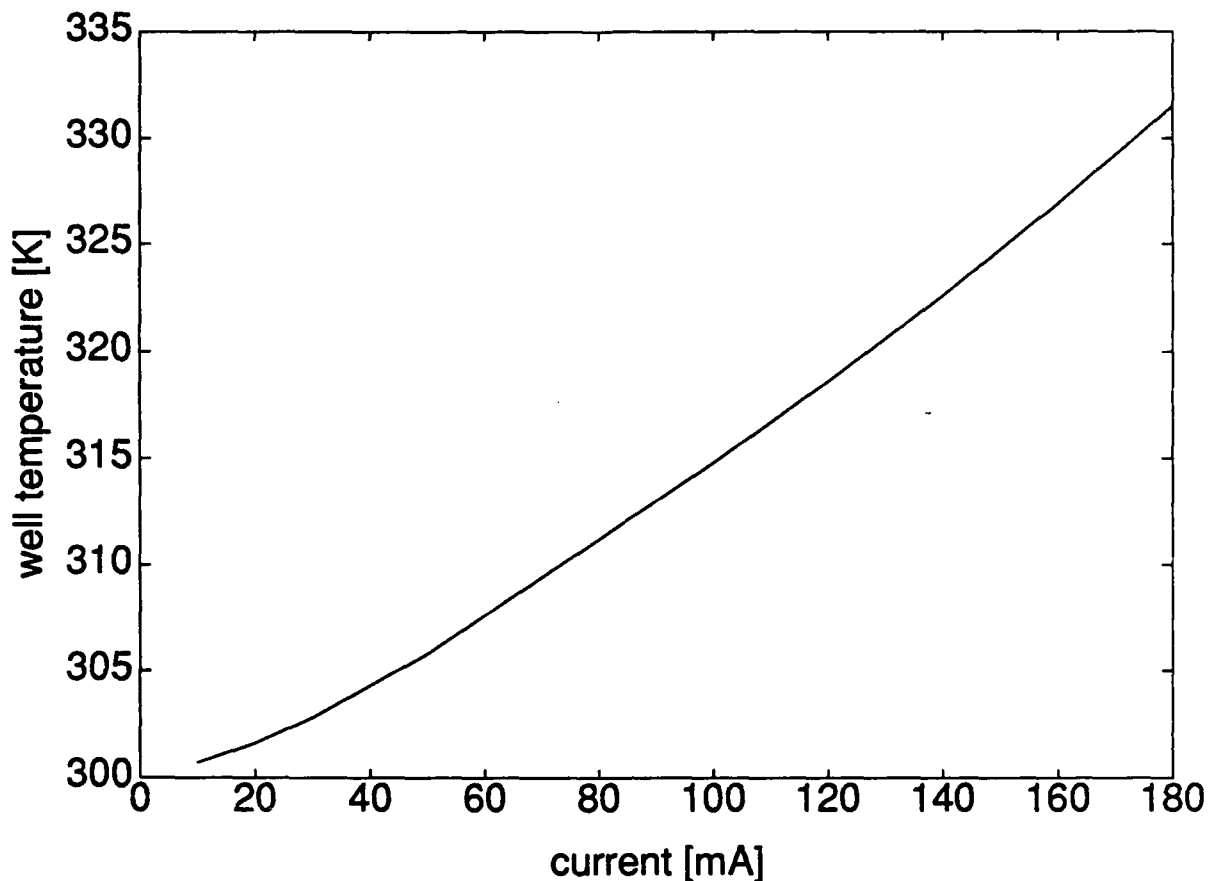
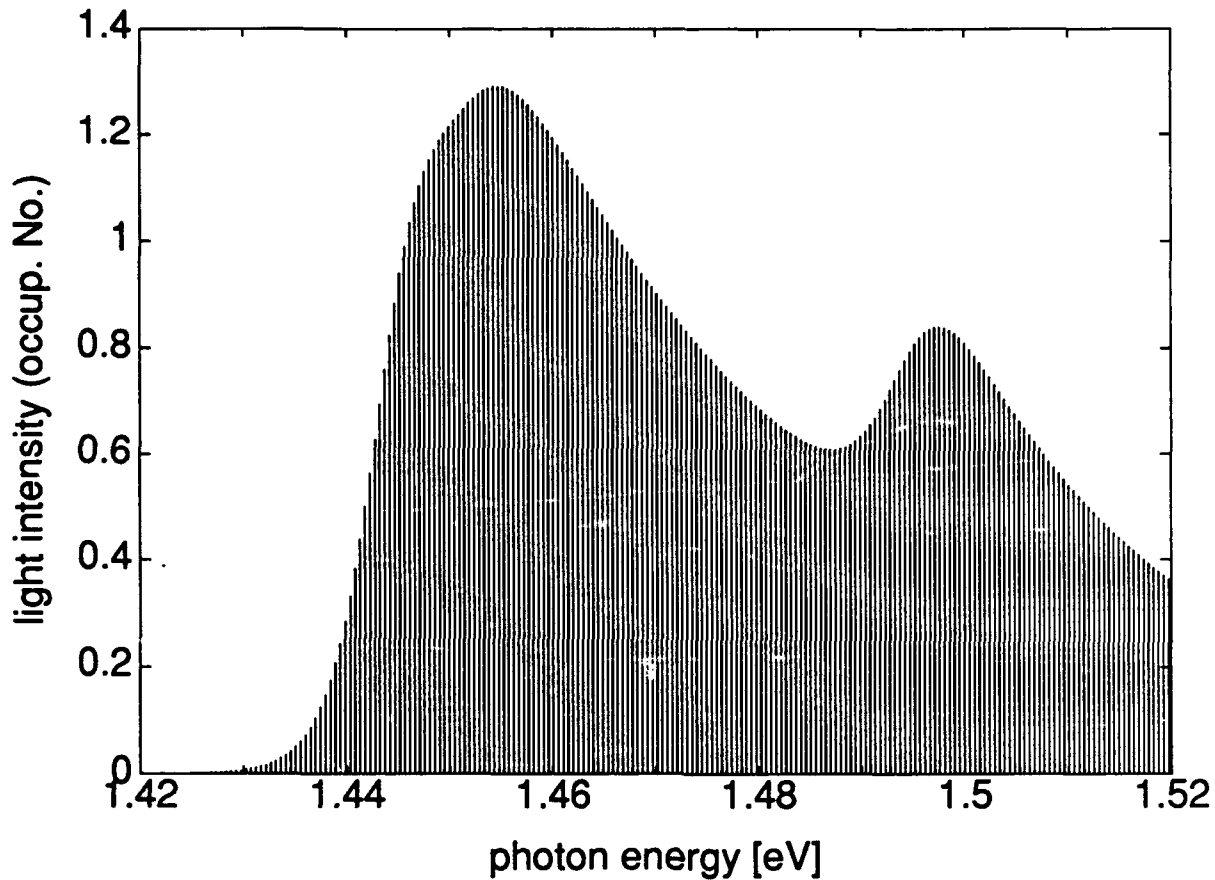


Figure 2.9: Approximate lattice temperature in the well.

gain coefficient (G_ν/v_g with G_ν in (2.11) and the group velocity v_g) curves show the gain saturation effect above the threshold. Also, the gain curve shifts to the lower energy spectrum as the current increases because the band gap changes due to increasing temperature at the quantum well. The temperature in the middle of the quantum well is shown in Figure 2.9. The free carrier loss is obtained from a numerical integration as in (2.23), and the value is about 2.0 cm^{-1} above threshold. The waveguide scattering loss is still an unknown fitting parameter. We have chosen a typical value, 5.0 cm^{-1} , from literature [47].

Users of MINILASE can optionally choose the staircase-like density of states for the region assigned to be a quantum well with quasi-two-dimensional electron and hole gases. The resulting gain and mode spectra from the staircase-like density of states are shown



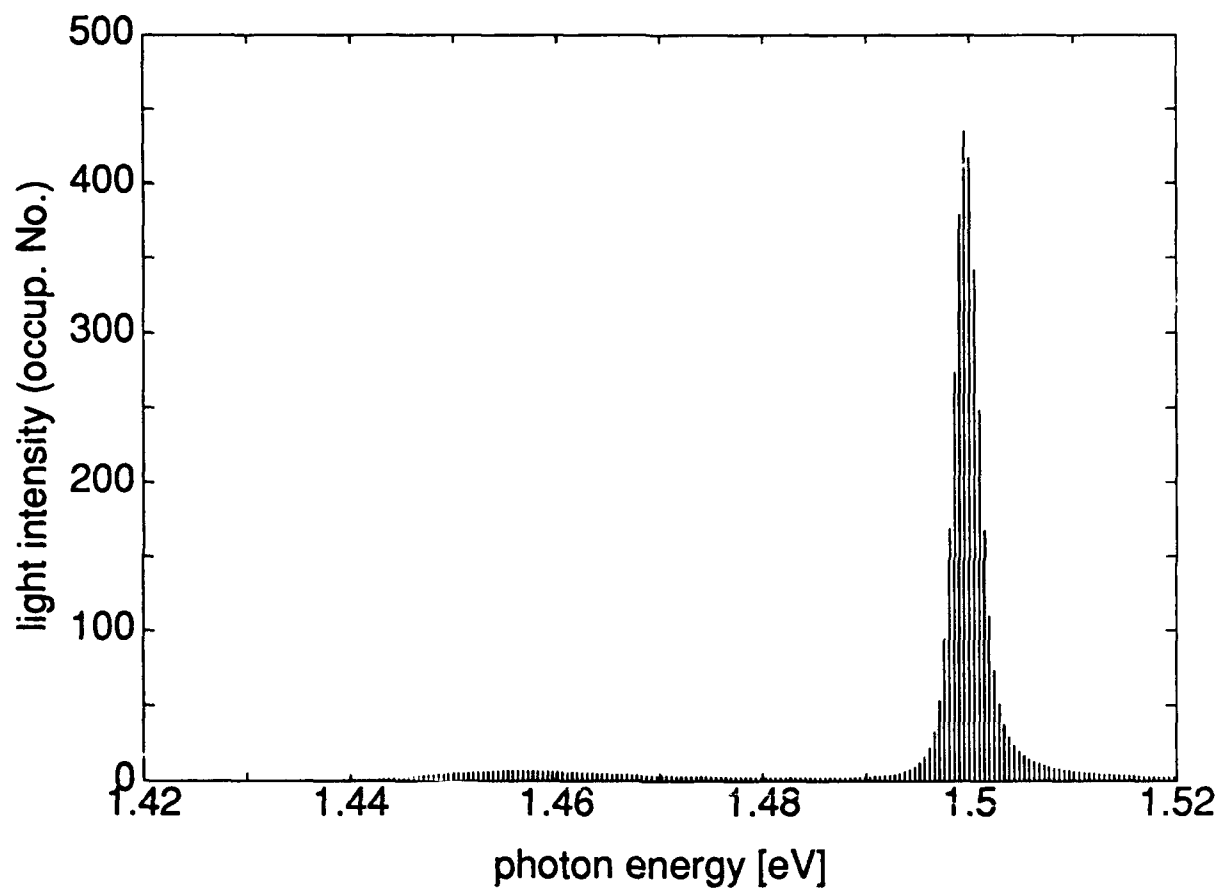
(a)

Figure 2.10: Spectra of photon numbers of fundamental-longitudinal modes at various pumping levels. A staircase-like density of states for a quasi-two-dimensional electron gas is used. (a) 2 mA.

(continued on p. 44)

in Figures 2.8 and 2.10, respectively. These diagrams show size-quantization effects and the subband level which supports the stimulated emission.

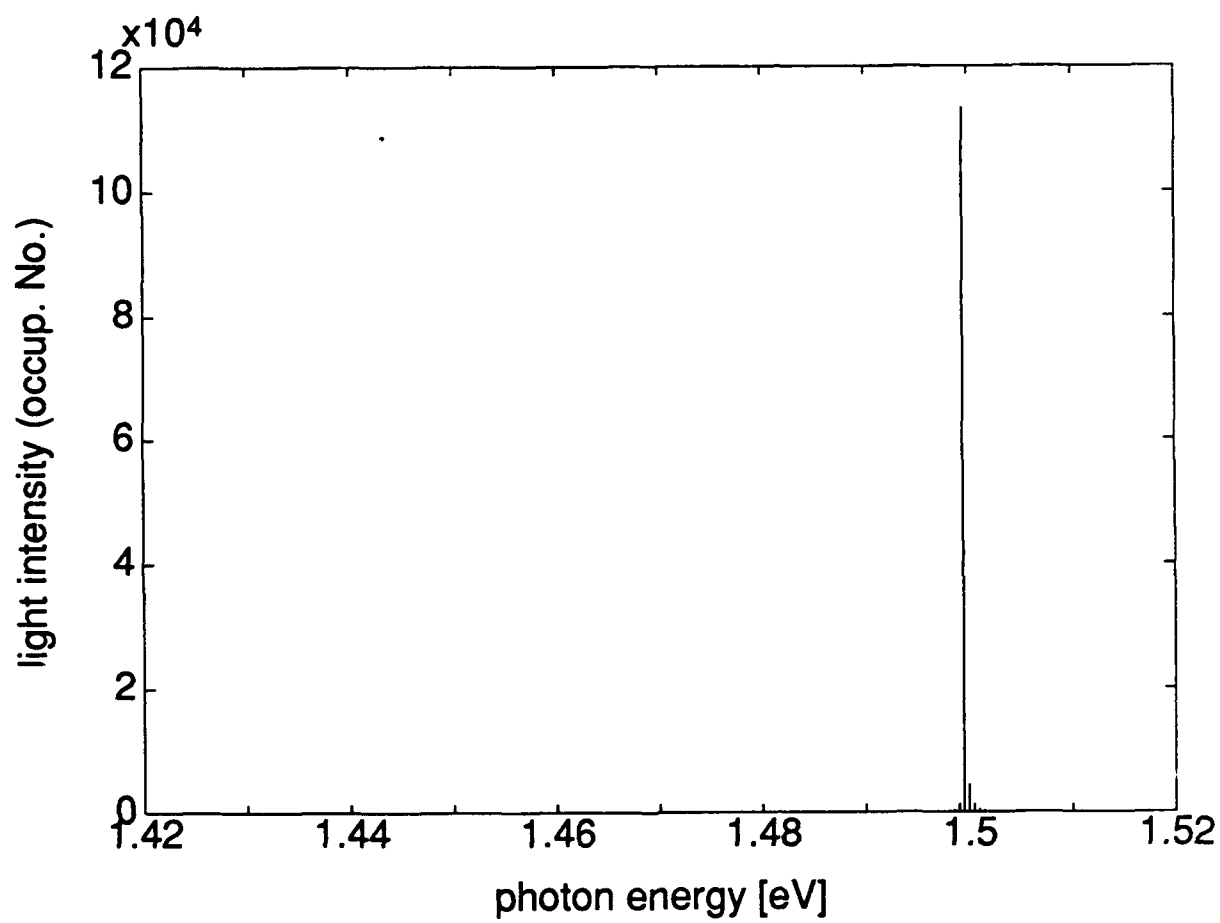
A mode development diagram can be obtained from the transient simulation, and is shown in Figure 2.11. We have assumed that the laser is driven from 2 mA abruptly to 10 mA at $t = 0$ ns and from 10 mA back to 2 mA at $t = 7.5$ ns. The size of the time step has been set uniformly at 25 ps, which has been found to be adequately short. The figure shows the initial turn-on delay time of 0.9 ns and relaxation oscillations of the optical power for 2 ns. Also it shows that several modes develop their magnitudes



(b)

Figure 2.10: (continued) (b) 4 mA.

(continued on p. 45)



(c)

Figure 2.10: (continued) (c) 10 mA.

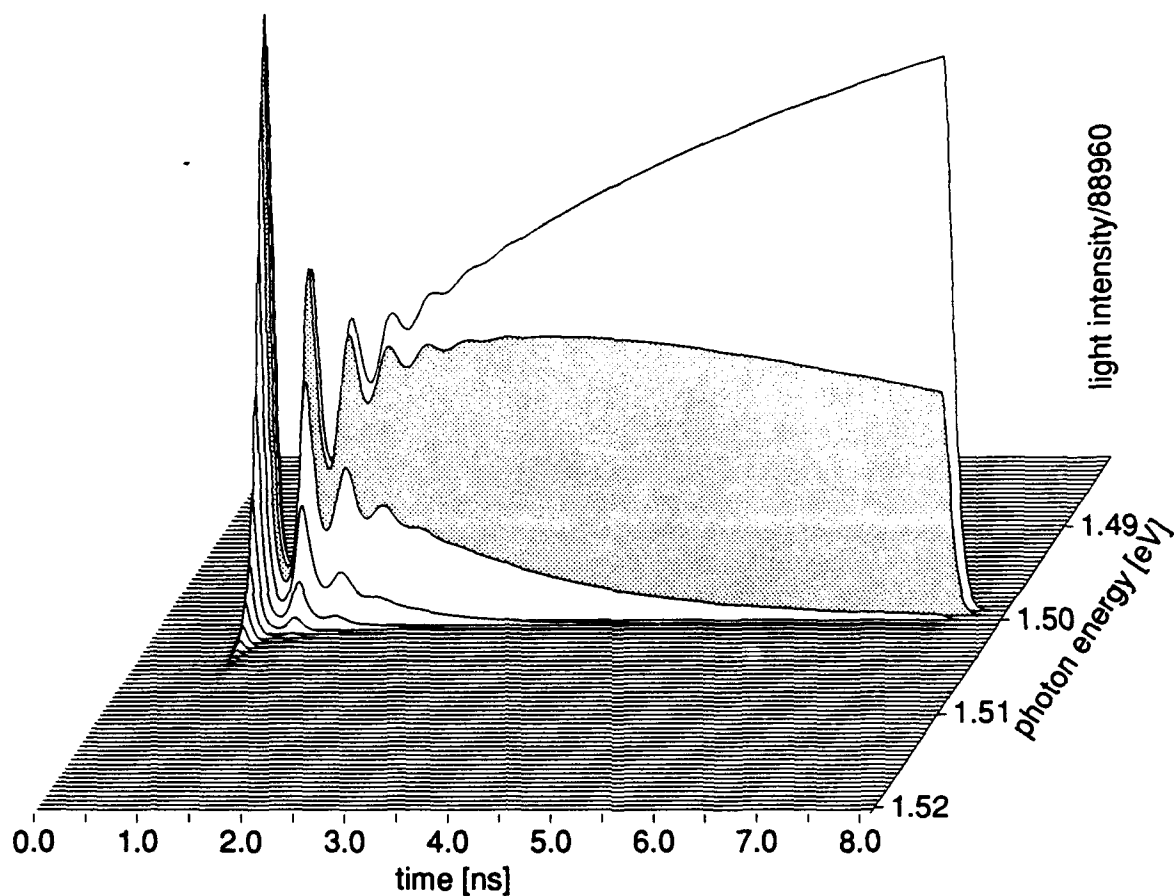


Figure 2.11: Both turn-on and turn-off transients in time. A series of current level change from 2 mA to 10 mA at $t = 0$ ns and from 10 mA back to 2 mA at $t = 7.5$ ns has been simulated. Each line represents intensity development of each mode. The central mode is denoted by half tone over the entire time scale to show its location in spectrum at the initial stage. The time step size of transient simulation has been set at 25 ps.

simultaneously at first, but only one mode has significant power in steady state. Also the center frequency and the spectral width change during the time development. The turn-on delay time and the period of relaxation oscillation depend on the various driving conditions of the laser. As is evident from the figure, the turn-off transient is negligibly short compared to the initial turn-on delay and the relaxation oscillation.

Figure 2.12 was obtained by applying a current step from 2 mA to 50 mA. The turn-on delay time has been shortened to 0.22 ns and the period of relaxation oscillation has become shorter than the case of Figure 2.11. In Figure 2.13, we show the time-development of carrier densities inside the quantum well. The magnitude of the initial peak in the optical power depends on the size of the time step taken for the time-dependent solution. This is because the whole procedure of the time-dependent solution is still not fully backward Euler, which was discussed in Sec. 2.4. Inadequately long time step gives an excess peak in the initial relaxation oscillation of the optical power. For instance, when we used the time step size of 5 ps instead of 2.5 ps for the current pulse of 2 – 50 – 2 mA sequence, we have observed the initial relaxation peak about 10 % larger than the peak observed with the time step size of 2.5 ps. One additional cause of the excessive peak in the initial relaxation oscillation could be because we have used a rate equation which averages out the intensity variation along the optical axis, and therefore ignores time required to sweep through the optical axis.

All these transient response characteristics are in good agreement with what experiments have suggested [78].

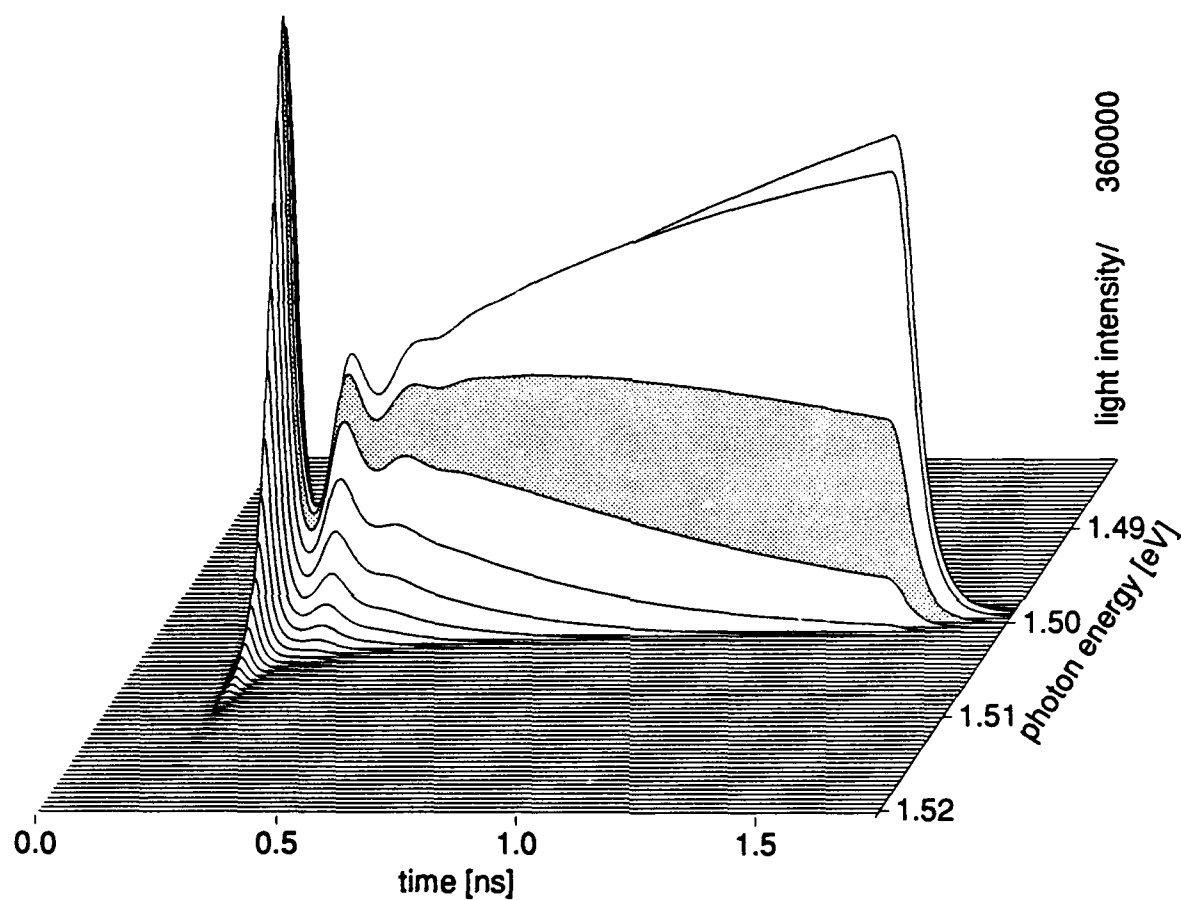
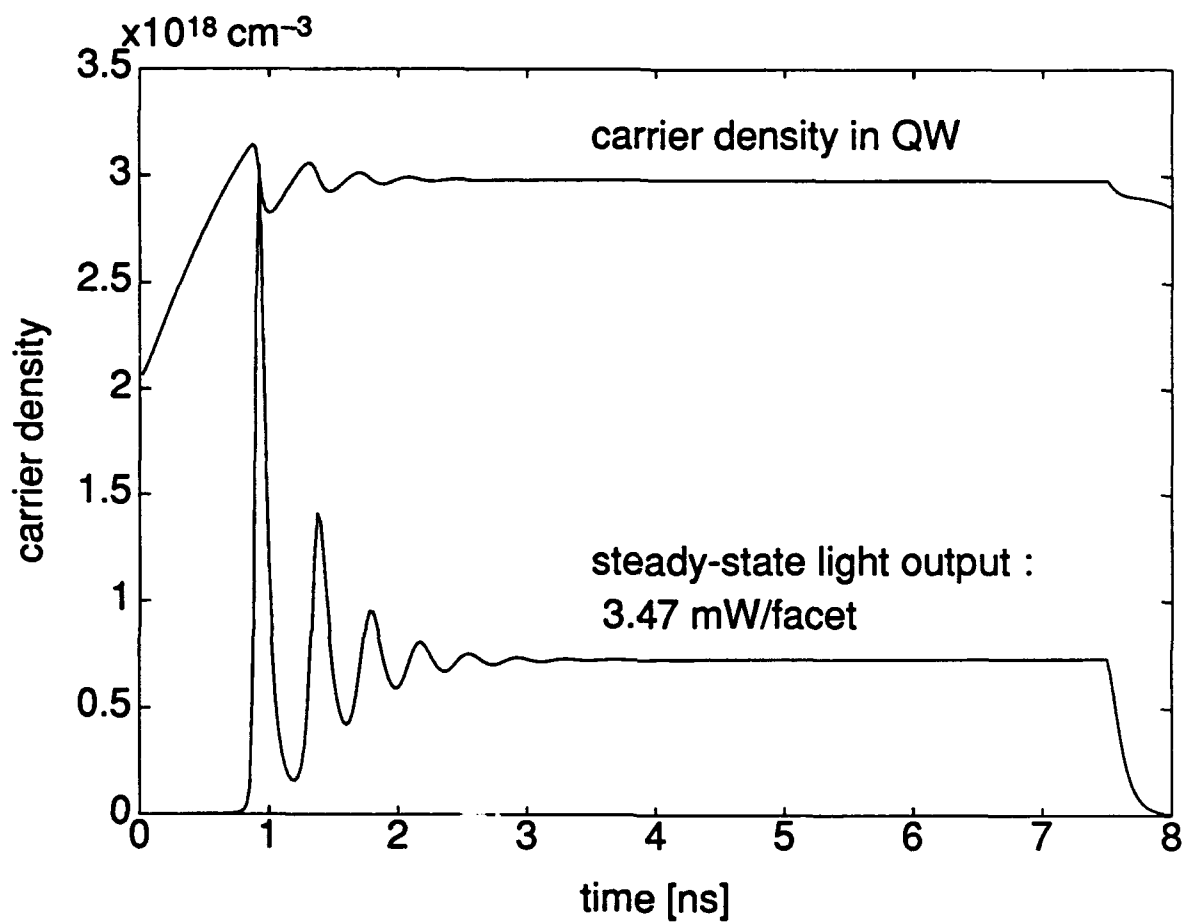
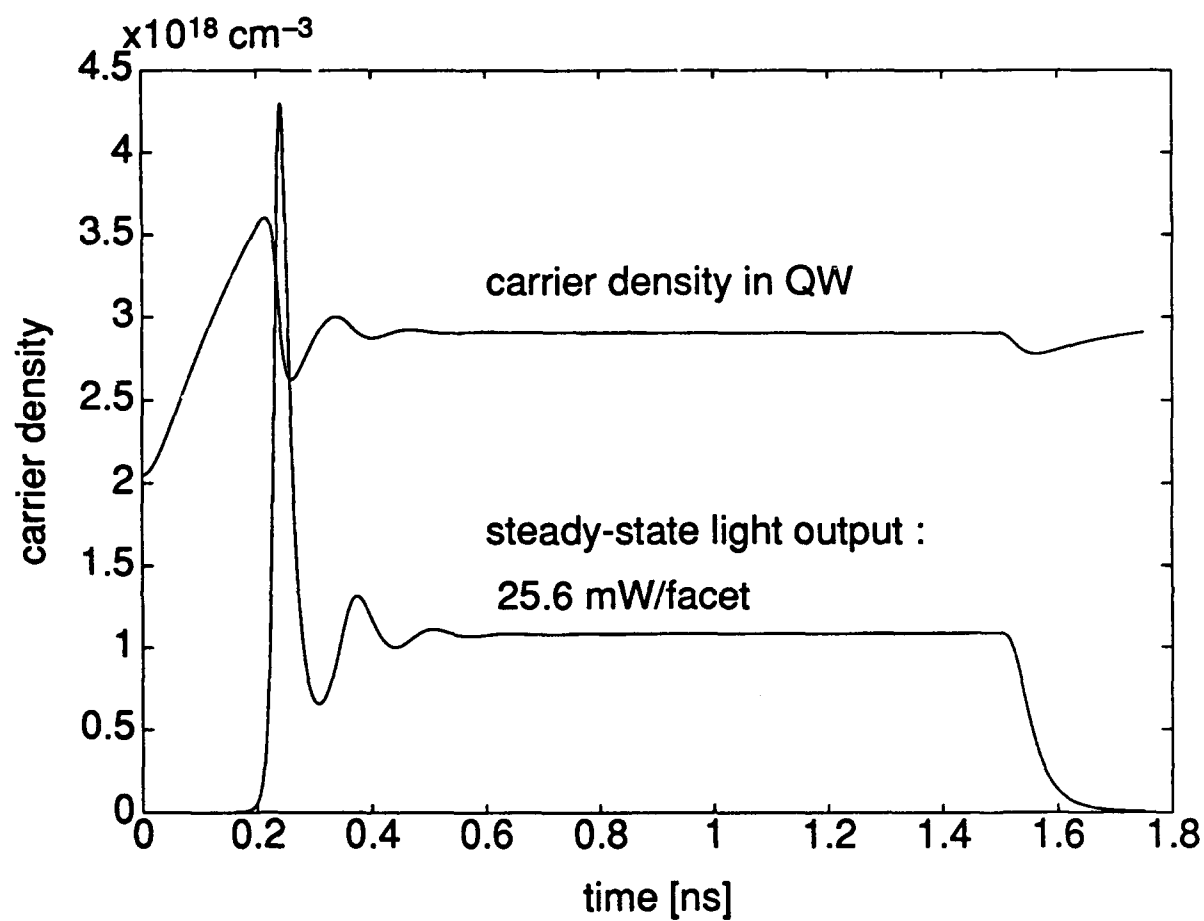


Figure 2.12: Both turn-on and turn-off transients in time. A series of current level change from 2 mA to 50 mA at $t = 0$ ns and from 50 mA back to 2 mA at $t = 1.5$ ns has been simulated. Each line represents intensity development of each mode. The mode distinguished from others by half-tone is the one which gives the peak at initial relaxation oscillation. The time step size is set at 2.5 ps.



(a)

Figure 2.13: Development of carrier densities ($n \simeq p$) in time in the middle of the quantum well in response to square pulses. The change of the laser light output is also shown with an arbitrary scale. (a) In response to a square pulse, 2 mA – 10 mA – 2 mA.
(continued on p. 50)



(b)

Figure 2.13: (continued) (b) In response to a square pulse, 2 mA – 50 mA – 2 mA.

CHAPTER 3

CONCLUSIONS

We have developed a two-dimensional simulator (MINILASE) which analyzes virtually all aspects of semiconductor laser operations. The simulator solves the device equations, heat flow equation, optical field equation, and the photon rate equation in a self-consistent manner. It gives all the solutions to the standard device equations and the resulting current flow diagrams and the temperature profile. It also generates the light-current curves, the optical field profile, the temperature profile, the spontaneous-emission spectrum, the optical output spectrum, and the gain spectrum.

In order to solve for the internal temperature distribution over the device cross section, the energy transfer in degenerate semiconductor devices has been examined, and the relevant differential equation has been solved together with the device equations. Proper inclusion of the Fermi-Dirac statistics has been found to be essential to obtain a differential equation which is linearly independent of the rest of the device equations. A set of novel expressions for the various fluxes has been suggested to account for the Fermi-Dirac statistics for the most important scattering mechanism, in which the scattering time is inversely proportional to the group velocity of carriers. Explicit formulas for the discretization of these fluxes have been found by extending the Scharfetter-Gummel scheme. There are many limitations in practical circumstances with regard to the boundary condition of the energy transport equation. A thorough treatment for the internal distribution of the temperature is a complex problem in which one needs to simulate the outside of the device as well as the inside.

Although derived under a series of assumptions and approximations, we think that the formalism presented in this thesis is general enough to be used in simulation of

heat transfer in many types of semiconductor devices, including heterojunction devices such as semiconductor lasers where local power consumption is an important factor for device performance. The algorithm presented here has been subjected to a series of experiments on a computer in the MINILASE project of the author, and results were given in Chapter 2.

We have presented the first two-dimensional simulation of the optical processes in a semiconductor laser using the rigorous Einstein coefficients of optical transition for individual Fabry-Perot modes of the laser resonator. Consequently, it is capable of simulating quantum-well lasers and their spectral responses. MINILASE is also the first attempt to use the full-Newton method for the system of equations obtained from discretization of the standard device equations and the heat flow equation. This enables us to analyze the temperature effect of a forward-biased semiconductor device self-consistently on various physical parameters such as the threshold current. Finally, MINILASE can obtain the two-dimensional transient-response including the initial relaxation oscillation of the individual Fabry-Perot mode intensities in a semiconductor laser.

The first priority of the MINILASE program has been a faithful implementation of physics, yet retaining versatility and flexibility of the program for a wide range of applications. We expect the simulator to be a useful design tool for optimizing semiconductor lasers as well as a useful research tool in quantum electronics laboratories.

APPENDIX A

ENERGY CONSERVATION FROM THE BOLTZMANN TRANSPORT EQUATION

Azoff [7] has derived the energy transport equation for the nonparabolic band structure from the classical Boltzmann transport equation (BTE) by taking the second moment (cited as the third moment in [7]). The same equation can be derived in a much simpler way by using an equivalent form of the BTE in which the velocity $\mathbf{v}_\mathbf{k}$ and the force $\mathbf{F}_\mathbf{k}$ follow the divergence symbols. Also, rather than taking the second moment for the standard equation, we can set up a version of BTE with respect to $(E_\mathbf{k} + E_C) f_\mathbf{k}$ for the electrons in the conduction band, since the total energy is conserved in much the same way as the total number of particles is conserved. In this way, no complication due to the nonparabolicity of the band appears in the derivation of the relation for the first law of thermodynamics. That is,

$$\begin{aligned} \frac{\partial}{\partial t} (E_C + E_\mathbf{k}) f_\mathbf{k} + \nabla_\mathbf{k} \cdot \frac{\mathbf{F}_\mathbf{k}}{\hbar} (E_C + E_\mathbf{k}) f_\mathbf{k} \\ + \nabla \cdot \mathbf{v}_\mathbf{k} (E_\mathbf{k} + E_C) f_\mathbf{k} = \left[\frac{\partial}{\partial t} (E_\mathbf{k} + E_C) f_\mathbf{k} \right]_{c,r} \end{aligned} \quad (\text{A.1})$$

The subscripts c and r stand for collision and recombination, respectively. Integrating this equation over the Brillouin zone in the reduced-zone scheme yields

$$\begin{aligned} \frac{\partial}{\partial t} (E_C n + u_e^{\text{kin}}) + \nabla \cdot (\mathbf{S}_e^{\text{kin}} + E_C \mathbf{j}_e) = \int_{\text{Bz}} E_\mathbf{k} \left(\frac{\partial f_\mathbf{k}}{\partial t} \right)_{c,r} \frac{d^3 \mathbf{k}}{4\pi^3} \\ - E_C (U_{\text{HSR}} + U_{\text{Aug}} + U_{\text{rad}}), \end{aligned} \quad (\text{A.2})$$

which then reduces to (1.1). Here u_e^{kin} and $\mathbf{S}_e^{\text{kin}}$ can be identified as the kinetic energy density and the kinetic energy flux of electrons, respectively. Substituting (1.15) into

(A.2) yields the standard equation.

$$\frac{\partial u_e^{\text{kin}}}{\partial t} + \nabla \cdot \mathbf{S}_e^{\text{kin}} + \nabla E_C \cdot \mathbf{j}_e = \int_{B_z} E_{\mathbf{k}} \left(\frac{\partial f_{\mathbf{k}}}{\partial t} \right)_{c,r} \frac{d^3 \mathbf{k}}{4\pi^3}. \quad (\text{A.3})$$

Note that the conserved quantity is not just the internal energy, but the kinetic energy which is the internal energy plus $\int_{B_z} (E_{\mathbf{k}} - E_{\mathbf{k}-\bar{\mathbf{k}}}) f_{\mathbf{k}} d^3 \mathbf{k} / 4\pi^3$. Note also that this expression explicitly separates out the Joule heat from the total energy flux in (1.1). A source of ill-conditioning in possible implementations of this term is in the form of an inner product of the two gradients [79].

APPENDIX B

EXPRESSIONS FOR THE HEAT FLUX

B.1 From Relaxation-Time Approximation

The integral expression for the energy flux from electrons is

$$\mathbf{S}_e = \int_{\mathbf{B}_z} \mathbf{v}_k (E_k + E_C) f_k \frac{d^3 k}{4\pi^3} = \mathbf{S}_e^{\text{kin}} + E_C \mathbf{j}_e. \quad (\text{B.1})$$

From the relaxation-time approximation, the probability distribution function f_k satisfies [12]

$$f_k^+ \equiv (f_k + f_{-k})/2, \quad f_k^- \equiv (f_k - f_{-k})/2, \quad (\text{B.2})$$

$$f_k^- = -\tau_k (\partial/\partial t + \mathbf{v}_k \cdot \nabla - \nabla E/\hbar \cdot \nabla_k) f_k^+. \quad (\text{B.3})$$

We obtain f_k^- by approximately equating f_k^+ in the right-hand side of (B.3) to the Fermi distribution,

$$f_F(T_c) \equiv \{\exp[(E_k + E_C - F_e)/T_c] + 1\}^{-1},$$

where T_c is the adjusted electron temperature for nonequilibrium under the influence of an electric field [12]. With this f_k^- , we obtain the following expression for \mathbf{S}_e in (B.1) [5] as

$$\mathbf{S}_e^{\text{kin}} = \mathbf{I}_1, \quad \mathbf{j}_e = \mathbf{I}_0, \quad (\text{B.4})$$

$$\mathbf{I}_j = - \int_{\mathbf{B}_z} \tau_k \mathbf{v}_k E_k^j \mathbf{v}_k \cdot \left(\nabla F_e + \frac{E - F_e}{T_c} \nabla T_c \right) \frac{\partial f_F}{\partial E_k} \frac{d^3 k}{4\pi^3}, \quad (\text{B.5})$$

The relaxation times for various scattering mechanisms as functions of velocity or kinetic energy of electrons can be found, e.g., in [8], [12], and [80].

Consider now a case where the relaxation time is proportional to $|\mathbf{v}_{\mathbf{k}}|^{-1}$.

$$\tau_{\mathbf{k}} = \frac{\bar{\tau}}{|\mathbf{v}_{\mathbf{k}}|}, \quad |\mathbf{v}_{\mathbf{k}}| = \frac{1}{\hbar} \frac{\partial E_{\mathbf{k}}}{\partial k}, \quad k = |\mathbf{k}|, \quad (\text{B.6})$$

where $\bar{\tau}$ is velocity-independent. As considered by Stratton [1] with $\mathbf{v}_{\mathbf{k}} = \hbar \mathbf{k} / m_e$, the above form is particularly suited for such materials as moderately-doped Si and Ge, where acoustic phonon scattering represents a major scattering mechanism. For moderately-doped III-V semiconductors where optical phonon scattering is predominant, the relaxation-time approximation with (B.6) is not strictly valid [12], [80], although still a good approximation at high temperatures [12]. Notice that ionized impurity scattering follows the same velocity dependence for the case of heavy screening, since in this limit the scattering potential is of short range [12]. Therefore, for laser application, factoring out $|\mathbf{v}_{\mathbf{k}}|^{-1}$ appears to be an excellent approximation, at least as long as the experimental mobility exhibits degrading with increasing temperature and with increasing carrier densities.

Following Kane [48], Nag and Chakravarti [81] derived an approximate relation between k^2 and $E_{\mathbf{k}}$ of an isotropic band structure under the assumption that $E_{\mathbf{k}} \ll E_G$:

$$\hbar^2 k^2 / 2m_e = E_{\mathbf{k}} (1 + \alpha_e E_{\mathbf{k}}). \quad (\text{B.7})$$

The analytic expression for the nonparabolicity α_e is given in the literature for various semiconductors [82], [44], [83]. Then, (B.5) becomes

$$\begin{aligned} I_j &= -\frac{2m_e \bar{\tau}}{3\pi^2 \hbar^3} \int_0^\infty (E_{\mathbf{k}}^{j+1} + \alpha_e E_{\mathbf{k}}^{j+2}) \\ &\quad \times \left(\nabla E_C + T_c \nabla \eta_e + \frac{E_{\mathbf{k}}}{T_c} \nabla T_c \right) \frac{\partial f_F}{\partial E_{\mathbf{k}}} dE_{\mathbf{k}} \\ &= M_e \left\{ [T_c^j (j+1)! \mathcal{F}_j(\eta_e) + \alpha_e T_c^{j+1} (j+2)! \mathcal{F}_{j+1}(\eta_e)] \right. \\ &\quad \times (\nabla E_C + T_c \nabla \eta_e) + [T_c^j (j+2)! \mathcal{F}_{j+1}(\eta_e) \\ &\quad \left. + \alpha_e T_c^{j+1} (j+3)! \mathcal{F}_{j+2}(\eta_e)] \nabla T_c \right\}. \end{aligned} \quad (\text{B.8})$$

$$M_e(T_c) = \frac{2m_e}{3\pi^2\hbar^3} \bar{\tau} T_c,$$

and the electron particle flux and the energy flux are given by

$$\begin{aligned} \mathbf{j}_e = & -M_e \{ [\mathcal{F}_0(\eta_e) + 2\alpha_e \mathcal{F}_1(\eta_e)] (\nabla E_C + T_c \nabla \eta_e) \\ & + [2\mathcal{F}_1(\eta_e) + 6\alpha_e \mathcal{F}_2(\eta_e)] \nabla T_c \}, \end{aligned} \quad (\text{B.9})$$

$$\begin{aligned} \mathbf{S}_e = & E_C \mathbf{j}_e - M_e T_c \{ [2\mathcal{F}_1(\eta_e) + 6\alpha_e \mathcal{F}_2(\eta_e)] (\nabla E_C + T_c \nabla \eta_e) \\ & + [6\mathcal{F}_2(\eta_e) + 24\alpha_e \mathcal{F}_3(\eta_e)] \nabla T_c \}, \end{aligned} \quad (\text{B.10})$$

respectively.

With this expression for the energy flux, we can separate the energy flux into a component which is carried by particle flux and the thermal conduction which is independent of particle transfer, by rewriting (B.10) as

$$\mathbf{S}_e = E_C \mathbf{j}_e + 2\Gamma_e T_c \mathbf{j}_e - K_e \nabla T_c, \quad (\text{B.11})$$

$$\begin{aligned} \Gamma_e &= \frac{\mathcal{F}_1 + 3\alpha_e \mathcal{F}_2}{\mathcal{F}_0 + 2\alpha_e \mathcal{F}_1}, \\ K_e &= M_e T_c \left\{ 6\mathcal{F}_2 + 24\alpha_e \mathcal{F}_3 - \frac{[2\mathcal{F}_1 + 6\alpha_e \mathcal{F}_2]^2}{\mathcal{F}_0 + 2\alpha_e \mathcal{F}_1} \right\}. \end{aligned} \quad (\text{B.12})$$

The thermal conductivity K_e reduces to $2T_c$ times the electrical conductivity for nondegenerate semiconductors as expected. For extreme degeneracy [10],

$$\mathcal{F}_j(\eta) \simeq \eta^{j+1}/(j+1)! + \pi^2 \eta^{j-1}/6j!, \quad \text{as } \eta \rightarrow \infty, \quad (\text{B.13})$$

K_e reduces to $\pi^2 T_c/3$ times the electrical conductivity, as in the case of a metal. Overall the thermal conductivity is proportional to T_c times the electrical conductivity in agreement with the Wiedemann-Franz law.

Equation (B.11) can be used for the simulation of semiconductors neglecting the last term when K_e is negligibly small compared to κ of the crystal lattice. There exists a possibility of an ill-conditioned matrix problem when Γ is very close to 1 (as in a nondegenerate region of a device) or almost constant (where the grid structure is too fine). Our conditioning treatment in Sec. 1.4 should be helpful in those cases.

As was pointed out in Ref. [13, p. 26], the term "heat flux" can be defined in various ways. The last term of (B.11), which represents "heat conduction," corresponds to one of many forms defining the heat flux of the electron *subsystem*. The heat flux S_e^Q of a single-component system is defined from a classical relation [13]:

$$S_e \equiv E_C j_e + u_e^{\text{kin}} j_e / n + (P_e + \Pi_e) \cdot j_e / n + S_e^Q, \quad (\text{B.14})$$

where P_e and Π_e are the so-called elastic stress tensor and the viscous stress tensor of electrons, respectively. This form is the basis of the hydrodynamic model of electron transfer in semiconductors.

Decomposition of total energy flux in (B.14) applies well only to the case of a classical electron gas, which supports the quadratic relationship between energy and crystal momentum. Explicit expressions for all energy flux components of degenerate electrons in the parabolic band structure can be found from the expression for the energy current given in (B.10) with $\alpha_e = 0$. For the heat flux, however, a phenomenological relation $S_e^Q \propto -\nabla T_e$ has been used in the previous literature [84], [85], [7].

For a multi-component system, the electronic heat flux is defined differently, and is equal to S_e^{kin} , since the total momentum of the whole system can be considered stationary (the total mass of conducting electrons being negligible to the total mass of the whole system). This electronic heat flux obviously has a convective energy flow component as stated in Ref. [2]. However, it is shown in Sec. B.2 that even the heat flux S_e^Q for the single-component system as in (B.14) may have a convective component of sizable magnitude which arises from particle diffusion in addition to the energy flow from the temperature gradient.

B.2 Heat Flux in the Hydrodynamic Model with the Relaxation-Time Approximation

To obtain expressions for carrier and energy fluxes in a binary system consisting of electrons and lattice, we have approximated the collision term of the BTE as

$$(\partial f_{\mathbf{k}}/\partial t)_c = -(f_{\mathbf{k}} - f^{\text{st}})/\tau_{\mathbf{k}}, \quad (\text{B.15})$$

so that the relaxation time $\tau_{\mathbf{k}}$ measures the characteristic time within which $f(\mathbf{r}, \mathbf{k})$ goes to a stationary distribution, f^{st} , at a certain space-momentum coordinate (\mathbf{r}, \mathbf{k}) . We then have equated f^{st} with $f_F(T_c)$, the *nondisplaced* Fermi distribution.

Note that in hydrodynamics of a gas of identical particles which mainly interact with themselves, the distribution function becomes approximately a displaced Maxwellian. This approximation is valid for an electron gas in which interaction between electrons and the crystal lattice is turned off, since electron-electron scattering will randomize the velocity distribution around the mean velocity. The equation obtained by inserting the displaced Maxwellian to f^{st} is not a usual form of relaxation-time approximation. However, the situation is a typical example in hydrodynamics, and there exists an asymptotic method of solution to a general BTE due to Enskog. According to this method, it has been shown, up to the second-order of Enskog's solution, that the heat flux does not have a convective component of energy flow, and the first-order expression becomes simply $\mathbf{S}_e^Q = -K_e \nabla T_c$ [87, p. 122].

However, the real situation of electrons in a solid is a two- or three-component system whose constituents have drastically different unit masses, so that the crystal lattice is virtually at rest. When other forms of scattering processes (e.g., electron-phonon scattering, ionized-impurity scattering) are dominant over the electron-electron scattering, we are led to think that the scattering will tend to randomize the velocity distribution of each component around the overall mean velocity of the *total* system. We may suppose that the real distribution function should be perturbed from the nondisplaced Maxwellian, so that one can use $f_F(T)$ for f^{st} in (B.15).

The electron-phonon scattering is indeed dominant over electron-electron scattering in a modestly doped semiconductor. In a degenerate semiconductor, electron-electron scattering accompanies and enhances the rate of other scattering processes (mostly electron-phonon scattering), making a second-order quantum-mechanical process [88]. The effect of high population makes it hard to tell whether the maximum distribution is displaced from the origin $\mathbf{k} = \mathbf{0}$ from the shape of the distribution function. Actually, extreme degeneracy (e.g., in a metal) makes the following discussion irrelevant, as is evident when we obtain the expression for the heat flux. Second, the relaxation time is hardly a constant over different energies, and the consequent effect on the resulting heat flux component in the energy flow in (B.14) comes not from higher than first order in $\tau_{\mathbf{k}}$, but from the first order in $\tau_{\mathbf{k}}$. The abnormality in distribution in \mathbf{k} -space caused by interaction of electrons with the crystal lattice gives heat flux, while nonuniformity of velocity distribution in real space gives viscosity. Therefore, the viscosity component of energy flux is usually negligible in electron transport except in a region of high transversal velocity difference as in an inversion layer of metal-oxide-semiconductor structure [89], for instance.

Since the stress tensors are defined as

$$P_e + \Pi_e \equiv \int_{B_z} \left(\mathbf{v}_{\mathbf{k}} - \frac{\mathbf{j}_e}{n} \right) \hbar (\mathbf{k} - \bar{\mathbf{k}}) f_{\mathbf{k}} \frac{d^3 \mathbf{k}}{4\pi^3}, \quad (\text{B.16})$$

we can then obtain an expression for the heat flux defined in (B.14) from the first-order solution for $f_{\mathbf{k}}$ to the BTE under the relaxation-time approximation. First, for the case that the relaxation time is velocity-independent,

$$\mathbf{S}_e^Q = -\frac{5}{2} M_e T_c \left(\frac{7}{2} \mathcal{F}_{\frac{3}{2}} - \frac{5}{2} \gamma_{\frac{3}{2}} \mathcal{F}_{\frac{1}{2}} \right) \nabla T_c. \quad (\text{B.17})$$

For the case of a relaxation time $\tau_{\mathbf{k}} \propto |\mathbf{v}_{\mathbf{k}}|^{-1}$, the remaining energy flux becomes to the first order in $\tau_{\mathbf{k}}$

$$\mathbf{S}_e^Q = -M_e T_c \left[\left(2\mathcal{F}_1 - \frac{5}{2} \gamma_{\frac{3}{2}} \mathcal{F}_0 \right) (\nabla E_C + T_c \nabla \eta_e) \right]$$

$$+ (6\mathcal{F}_2 - 5\gamma_{\frac{3}{2}}\mathcal{F}_1) \nabla T_c], \quad (\text{B.18})$$

while the viscosity component comes from a term of order $\tau_k \tau_u$. Note that it is possible that the total kinetic energy flow lags behind the convective energy flow with f_k obtained from the relaxation time $\tau_k \propto |\mathbf{v}_k|^{-1}$. Note that when we specified the relaxation time in the form (B.6) for the electron-lattice interaction, we also introduced a form of energy dissipation mechanism to the lattice system. We then again separate this lagging convective component of the heat flux as

$$\mathbf{S}_e^Q = -T_c \left(2\gamma_1 - \frac{5}{2}\gamma_{\frac{3}{2}} \right) \mathbf{j}_e - K_e \nabla T_c, \quad (\text{B.19})$$

where $K_e = M_e T_c (6\mathcal{F}_2 - 4\gamma_1 \mathcal{F}_1)$ as in (B.12) with $\alpha_e = 0$. Note that, for the case of extreme degeneracy as in a metal, the lagging convective component of heat flux again vanishes, leaving the heat conduction term only. This can be verified by evaluating $2\gamma_1 - \frac{5}{2}\gamma_{\frac{3}{2}}$ with the formula given in (B.13). Therefore, as the carrier density increases, choice between $f_M(\mathbf{k})$ and $f_M(\mathbf{k} - \bar{\mathbf{k}})$ for f^{st} in the relaxation-time approximation becomes irrelevant.

Most previous simulations on heat flow in semiconductor devices have been based on the expression for the electron energy flux given in the form (B.14) and $\mathbf{S}_e^Q = -K_e \nabla T_c$ with their varying approximations for the coefficient K_e [84], [90], [85], [86]. Though not clearly stated in these works, this conjecture was based on the assumption either that the electron gas in a solid can be approximated by a classical one-component gas (in which electron-electron scattering represents the major scattering mechanism) or that the first-order relaxation-time-approximation estimation on the heat flux gives a vanishing coefficient. When we take care of the two-component scattering system, we get heat flux component (lagging in the case of $\tau_k \propto |\mathbf{v}_k|^{-1}$ arising from major scattering processes, e.g., acoustic phonon scattering) which is proportional to the particle flux. We thus need to be aware of some subtraction of convective energy flow after the addition of the pressure component.

APPENDIX C

EXPRESSIONS FOR CARRIER FLUX

There are several equivalent expressions for the carrier fluxes and the energy flux for semiconductors with nonuniform band structure. Expressions (1.15) and (1.25) are based on the gradients of η_e (η_h) with those of E_C and T_c . We may even express the fluxes in terms of the gradients of F_e and T_c as shown in Sec. B.2. With $\alpha_e = 0$,

$$\mathbf{j}_e = -M_e \{ \mathcal{F}_0(\eta_e) \nabla F_e + [2\mathcal{F}_1(\eta_e) - \eta_e \mathcal{F}_0(\eta_e)] \nabla T_c \}. \quad (\text{C.1})$$

This form needs further transformation before the Scharfetter-Gummel scheme can be applied [24].

Another type of expression is that of Azoff [6] shown here for the nonuniform temperature distribution:

$$-q\mathbf{j}_e = \mu_e \nabla \gamma_{\frac{3}{2}} T_c n + \mu_e n \nabla E_C - \frac{3}{2} \mu_e n \gamma_{\frac{3}{2}} T_c \nabla \ln m_e. \quad (\text{C.2})$$

This form explicitly accounts for the force term due to an effective mass variation in space. He derived this expression from the momentum conservation relation with a momentum-relaxation time, which is assumed independent of energy. The suitable form for the Scharfetter-Gummel discretization scheme then becomes

$$\mathbf{j}_e = -\frac{\mu_e}{q} \left\{ \gamma_{\frac{3}{2}} T_c \nabla n + n \left[\nabla (E_C + \gamma_{\frac{3}{2}} T_c) - \frac{3}{2} \gamma_{\frac{3}{2}} T_c \nabla \ln m_e \right] \right\}. \quad (\text{C.3})$$

One can readily construct a formula similar to (1.27). This expression can be interpreted easily in a conventional way as we classify the flux components: the diffusion part and the drift part. The drift part comes not only from the conventional force $-\nabla E_C$, but

also from the negative gradient of the electron pressure—the median level of the electron internal energy—and an unusual nonconservative force from the nonuniformity of the band structure. This last term does not appear if we allow other forms than ∇n as the diffusion term as in (1.25). Note that when the real relaxation time is dependent on the kinetic energy, we cannot use the momentum conservation relation itself for the expression of carrier fluxes. Instead, we should evaluate the moment of $\mathbf{v}_k \tau_k$ for the BTE. Then we will get different coefficients and γ factors. If we extend Azoff's expression for the case of velocity-dependent relaxation time $\tau_k = \bar{\tau} / |\mathbf{v}_k|$ as in (B.6), we obtain

$$\begin{aligned}
 -\mathbf{j}_e = & \frac{2}{3} \frac{\bar{\tau}}{m_e} \nabla [m_e M_e T_c \mathcal{F}_1(\eta_e)] + \frac{2}{3} \frac{\bar{\tau}}{m_e} m_e M_e \mathcal{F}_0(\eta_e) \nabla E_C \\
 & - \frac{5}{3} \frac{\bar{\tau}}{m_e} m_e M_e T_c \mathcal{F}_1(\eta_e) \nabla \ln m_e.
 \end{aligned} \tag{C.4}$$

The choice of formulas for discretization is intimately coupled with the choice of independent variables for the system of equations. Among the options are F_e , η_e (or equivalently $\mathcal{F}_0(\eta_e)$), and n . (The so-called Slotboom variables are not well suited here.) Because of the wide decimal range of the carrier densities, the Scharfetter-Gummel discretization scheme appears to be a requirement. From the following considerations, we prefer the set of flux equations given in (1.25), whose counterpart flux equations are the kinetic energy fluxes. First, we can put all the explicit temperature dependencies in less than three terms. Second, using the Onsager-symmetric flux equations as in (1.15)–(1.20) makes the formulation simple and symmetric. The discretization scheme as introduced in Sec. 1.5 is relatively simple with our choice of flux equations (1.25)–(1.26). Choosing η_e and η_h as two independent variables gives considerable flexibility in handling terms arising from incomplete ionization of impurities and from various recombination rates, especially the radiative recombination rate in the quantum-well region.

Note the difference between the use of conventional mobilities, μ_e and μ_h , and the parameters used here, M_e and M_h . The theoretical definition of mobility is given in various textbooks and is a dyadic by nature. It is a function of band structure and the scattering mechanism through the scattering time. Use of any theoretical expression for

these parameters is usually discouraged in favor of phenomenological expressions which depend on the carrier densities, impurity densities, and temperature. Thus, there is no restriction against using a new expression for such parameters as long as we can transform those available experimental expressions into ones that conform to our definition by such relations as (1.17). In fact, the new mobility parameters with $\mathcal{F}_0(\eta)$ actually more closely represent the situation in a semiconductor device in its degenerate state. Moreover, the new parameters are often less temperature dependent than the conventional ones [91].

For the Newton iteration, it is critical to have analytic expressions for the Fermi-Dirac integrals ($\mathcal{F}_j(\eta)$), their derivatives, and the inverse function for at least one of those Fermi-Dirac integrals. Availability of closed-form expression for the zeroth-order Fermi-Dirac integral, $\mathcal{F}_0(\eta) = \ln(e^\eta + 1)$ and its inverse function $\mathcal{F}_0^{-1}(N) = \ln(e^{-N} - 1)$ deserve mention with the special property $\frac{d}{d\eta}\mathcal{F}_j(\eta) = \mathcal{F}_{j-1}(\eta)$ for our emphasis on integer-order integrals for flux expressions. Available analytic expressions for various-order Fermi-Dirac integrals were reviewed in [92] with their analytic properties.

LIST OF REFERENCES

- [1] R. Stratton, "Semiconductor current-flow equations (diffusion and degeneracy)," *IEEE Trans. Electron Devices*, vol. 19, pp. 1288-1292, 1972.
- [2] K. Bløtekjær, "High-frequency conductivity, carrier waves and acoustic amplification in drifted semiconductor plasmas," *Ericson Technics*, vol. 22, pp. 125-183, 1966.
- [3] v. M. Kohler, "Untersuchungen über die elektrischen und thermischen Erscheinungen im Magnetfeld unter besonderer Berücksichtigung der Frage nach der Reversibilität der thermoelektrischen Effekte," *Anal. Phys.*, 5. Folge., Band 40, pp. 601-627, 1941.
- [4] C. Herring, "Theory of the thermodynamic power of semiconductors," *Phys. Rev.*, 2nd ser., vol. 96, pp. 1163-1187, 1954.
- [5] A. H. Marshak and K. M. van Vliet, "Electrical current in solids with position-dependent band structure," *Solid-State Electron.*, vol. 21, pp. 417-427, 1978.
- [6] E. M. Azoff, "Generalized energy-momentum conservation equations in the relaxation time approximation," *Solid-State Electron.*, vol. 30, pp. 913-917, 1987.
- [7] E. M. Azoff, "Semiclassical high-field transport equations for nonparabolic heterostructure degenerate semiconductors," *J. Appl. Phys.*, vol. 64, pp. 2439-2446, 1988.
- [8] A. H. Wilson, *The Theory of Metals*. 2nd ed. Cambridge: Cambridge at the Univ. Press, 1953.
- [9] J. M. Ziman, *Electrons and Phonons*. London: Oxford University, 1962.
- [10] P. S. Kireev, *Semiconductor Physics*, Engl. ed. Moscow: Mir, 1974.
- [11] J. M. Luttinger, "4. Transport theory" in *Mathematical Methods in Solid State and Superfluid Theory*, ed., R. C. Clark and G. H. Derrick, Plenum, New York, pp. 157-193, 1967.
- [12] K. Hess, *Advanced Theory of Semiconductor Devices*. Englewood Cliffs, N.J.: Prentice Hall, 1988.

- [13] S. R. de Groot and P. Mazur, *Non-Equilibrium Thermodynamics*. Amsterdam: North Holland, 1962, New York: Dover, 1984.
- [14] S. Selberherr, *Analysis and Simulation of Semiconductor Devices*. New York: Springer, 1984.
- [15] D. P. Wilt and A. Yariv, "A self-consistent static model of the double-heterostructure laser," *IEEE J. Quantum Electron.*, vol. QE-17, pp. 1941-1951, 1981.
- [16] T. Kumar, R. F. Ormondroyd, and T. E. Ozzi, "A self-consistent model of the lateral behavior of a twin-stripe injection laser," *IEEE J. Quantum Electron.*, vol. QE-22, pp. 1975-1985, 1986.
- [17] T. Ohtoshi, K. Yamaguchi, C. Nagaoka, T. Uda, Y. Murayama, and N. Chinone, "Two-dimensional device simulator of semiconductor lasers," *Solid-State Electron.*, vol. 30, pp. 627-638, 1987.
- [18] K. Kahen, "Two-dimensional simulation of laser-diodes in the steady state," *IEEE J. Quantum Electron.*, vol. 24, pp. 641-651, 1988.
- [19] S. Seki, M. Tomizawa, K. Yokoyama, and Y. Yoshii, "Two-dimensional, static, and dynamic device simulation of laser diodes," in *Tech. Dig. Int. Electron Devices Meeting*, 1988.
- [20] R. S. Varga, *Matrix Iterative Analysis*. Englewood Cliffs, N. J.: Prentice-Hall, 1962.
- [21] D. L. Scharfetter and H. K. Gummel, "Large-scale analysis of a silicon read diode oscillator," *IEEE Trans. Electron Devices*, vol. ED-16, pp. 64-77, 1969.
- [22] T.-W. Tang, "Extension of the Scharfetter-Gummel algorithm to the energy balance equation," *IEEE Trans. Electron Devices*, vol. ED-31, pp. 1912-1914, 1984.
- [23] C. C. McAndrew, K. Singhal, and E. L. Heasell, "A consistent nonisothermal extension of the Scharfetter-Gummel stable difference approximation," *IEEE Electron Devices Lett.*, vol. EDL-6, pp. 446-447, 1985.
- [24] M. S. Lundstrom, R. J. Schwartz, and J. L. Gray, "Transport equations for the analysis of heavily doped semiconductor devices," *Solid-State Electron.*, vol. 24, pp. 195-202, 1981.
- [25] R. Stratton, "Diffusion of hot and cold electrons in semiconductor barriers," *Phys. Rev.*, vol. 126, pp. 2002-2014, 1962.
- [26] E. M. Lifshitz and L. P. Pitaevskii, *Physical Kinetics*, Engl. ed. Oxford: Pergamon, 1981.
- [27] W. T. Tsang, R. A. Logan, and J. A. Ditzenberger, "Ultra-low threshold graded-index waveguide, separate confinement, CW buried heterostructure lasers," *Electron. Lett.*, vol. 18, pp. 845-847, 1982.

- [28] G. B. Hocker and W. K. Burns, "Mode dispersion in diffused channel waveguides by the effective index method," *Appl. Opt.*, vol. 16, pp. 113-118, 1977.
- [29] R. Dingle, W. Wiegmann, and C. H. Henry, "Quantum states of confined carriers in very thin $\text{Al}_x\text{Ga}_{1-x}\text{As-GaAs-Al}_x\text{Ga}_{1-x}\text{As}$ heterostructures," *Phys. Rev. Lett.*, vol. 33, pp. 827-830, 1974.
- [30] T. P. Pearsall, R. E. Nahory, and J. R. Chelikowsky, in *Gallium Arsenide and Related Compounds, Inst. Phys. Conf. Ser.*, vol. 33b, L. Eastman, Ed., pp. 331-338, 1977.
- [31] A. Haug, "Auger recombination in direct-gap semiconductors: band-structure effects," *J. Phys. C: Solid State Phys.*, vol. 16, pp. 4159-4127, 1983.
- [32] W. Lochman, "Scattering mechanism in phonon-assisted Auger-recombination," *Phys. Stat. Sol. Ser. (a)*, vol. 42, pp. 181-185, 1977. (The minority carrier lifetimes for various phonon-assisted CCCH processes (such as τ_p^{NPO}) were grossly underestimated by several orders of magnitude compared to those of phonon-assisted CHHS processes in this paper. See [33].)
- [33] W. Bardyszewski and D. Yevick, "Compositional dependence of the Auger coefficient for InGaAsP lattice matched to InP," *J. Phys.*, vol. 58, pp. 2713-2723, 1985.
- [34] M. Takeshima, "Phonon-assisted Auger recombination in a quasi-two-dimensional structure semiconductors," *Phys. Rev. B*, vol. 30, pp. 3302-3308, 1984.
- [35] A. Sugimura, "Structure-dependent threshold current density in InGaAsP quantum well lasers," *Appl. Phys. Lett.*, vol. 42, pp. 17-19, 1983.
- [36] R. Olshansky, C. B. Su, J. Manning, and W. Powazinik, "Measurement of radiative and nonradiative recombination rates in InGaAsP and AlGaAs light sources," *IEEE J. Quantum Electron.*, vol. QE-20, pp. 838-854, 1984.
- [37] B. L. Gel'mont, Z. N. Sokolova, and I. N. Yassievich, "Auger recombination in direct-gap *p*-type semiconductors," *Sov. Phys. Semicond.*, vol. 16, pp. 382-387, 1982.
- [38] J. Jastrzebski, J. Logowski, H. C. Gatos, and W. Walukiewicz, in *Inst. Phys. Ser. No. 45: Proc. the 7th Int. Symp. on Gallium Arsenide and Related Compounds*, C. M. Wolfe, Ed., 1979, pf. 437.
- [39] M. Takeshima, "Unified theory of the impurity and phonon scattering effects on Auger recombination in semiconductors," *Phys. Rev. B*, vol. 25, pp. 5390-5414, 1982.
- [40] C. D. Thurmond, "The standard thermodynamic functions for the formation of electrons and holes in Ge, Si, GaAs, and GaP," *J. Electrochem. Soc.*, vol. 122, pp. 1133-1141, 1975.

- [41] I. Balslev, "Optical absorption due to inter-conduction-minimum transitions in gallium arsenide," *Phys. Rev.*, vol. 173, pp. 172-766, 1968.
- [42] C. Maziar, "Material models and device structures for GaAs solar cells," Solar Energy Res. Inst. Subcontract Rep. No. XL-3-03124-1, 1984.
- [43] J. D. Wiley, "Chap. 2. Mobility of holes in III-V compounds," in *Semiconductors and Semimetals*, vol. 10, R. K. Willardson and A. C. Beer, Eds. 1975, pp. 91-174. (Reviewed in [44].)
- [44] J. S. Blakemore, "Semiconducting and other major properties of gallium arsenide," *J. Appl. Phys.*, vol. 53, pp. R123-R181, 1982.
- [45] J. Manning, R. Olshansky, and C. B. Su, "The carrier-induced index change in a AlGaAs and 1.3 μm InGaAsP diode lasers," *IEEE J. Quantum Electron.*, vol. QE-19, pp. 1525-1530, 1983.
- [46] T. L. Paoli, "Wave guiding in a stripe-geometry junction lasers," *IEEE J. Quantum Electron.*, vol. QE-13, pp. 662-668, 1977.
- [47] H. C. Casey, Jr. and M. B. Panish, *Heterostructure Lasers, Part A*. New York: Academic, 1978.
- [48] E. O. Kane, "Band structure of indium antimonide," *J. Phys. Chem. Solids*, vol. 1, pp. 249-261, 1957.
- [49] G. Lasher and F. Stern, "Spontaneous and stimulated recombination radiation in semiconductors," *Phys. Rev.*, vol. 133, pp. A533-A563, 1964.
- [50] A. Sugimura, "Threshold currents for AlGaAs quantum well lasers," *IEEE J. Quantum Electron.*, vol. QE-20, pp. 336-343, 1984.
- [51] P. T. Landsberg, M. S. Abrahams, and M. Osinski, "Evidence of no k -selection in gain spectra of quantum well AlGaAs laser diodes," *IEEE J. Quantum Electron.*, vol. QE-21, pp. 24-28, 1985.
- [52] K. Hess, B. A. Vojak, N. Holonyak, Jr., and R. Chin, "Temperature dependence of threshold current for a quantum-well heterostructure laser," *Solid-State Electron.*, vol. 23, pp. 585-589, 1980.
- [53] M. Yamanishi and Y. Lee, "Phase damping of optical dipole moments and gain spectra in semiconductor lasers," *IEEE J. Quantum Electron.*, vol. QE-23, pp. 367-370, 1987.
- [54] M. Asada, "Intraband relaxation time in quantum-well lasers," *IEEE J. Quantum Electron.*, vol. 25, pp. 2019-2026, 1989.

- [55] M. Yamanishi and I. Suemune, "Comment on polarization dependent momentum matrix elements in quantum well lasers," *Jpn. J. Appl. Phys.*, vol. 23, pp. L35-L36, 1984.
- [56] T. Ikegami, "Reflectivity of mode at facet and oscillation mode in double-heterostructure injection lasers," *IEEE J. Quantum Electron.*, vol. QE-8, pp. 470-476, 1972.
- [57] Y. P. Varshni, "Temperature dependence of the energy gap in semiconductors," *Physica*, vol. 34, pp. 149-154, 1967.
- [58] G. A. Samara, "Temperature and pressure dependence of the dielectric constants of semiconductors," *Phys. Rev. B*, vol. 27, pp. 3494-3505, 1983.
- [59] R. E. Fern and A. Onton, "Refractive index of AlAs," *J. Appl. Phys.*, vol. 42, pp. 3499-3500, 1971.
- [60] M. Zvára, "Interband Faraday rotation in gallium arsenide," *Phys. Status Solidi*, vol. 27, pp. K157-K160, 1968.
- [61] B. Monemar, "Fundamental energy gaps of AlAs and AlP from photoluminescence excitation spectra," *Phys. Rev. B*, vol. 8, pp. 5711-5718, 1973.
- [62] D. L. Camphausen, G. A. N. Connell, and W. Paul, "Calculation of energy band pressure coefficient from the dielectric theory of the chemical bond," *Phys. Rev. Lett.*, vol. 26, pp. 184-188, 1971.
- [63] S. Adachi, "GaAs, AlAs, and $\text{Al}_x\text{Ga}_{1-x}\text{As}$: Material parameters for use in research and device applications," *J. Appl. Phys.* vol. 53, pp. R1-R29, 1985.
- [64] R. Dingle, R. A. Logan, and J. R. Arthur, Jr., in *Gallium Arsenide and Related Compounds*, Inst. Phys., London, pf. 210, 1970.
- [65] O. K. Kim and W. G. Spitzer, "Infrared reflectivity spectra and Raman spectra of $\text{Ga}_{1-x}\text{Al}_x\text{As}$ mixed crystals," *J. Appl. Phys.* vol. 50, pp. 4362-4370, 1979.
- [66] P. Lawaetz, "Valence-band parameters in cubic semiconductors," *Phys. Rev. B*, vol. 4, pp. 3460-3467, 1971.
- [67] A. L. Mears and R. A. Stradling, "Cyclotron resonance and Hall measurements of the hole carriers in GaAs," *J. Phys. C*, vol. 4, pp. L22-L26, 1971.
- [68] A. K. Saxena, "Electron mobility in $\text{Ga}_{1-x}\text{Al}_x\text{As}$ alloys," *Phys. Rev. B*, vol. 24, pp. 3295-3302, 1981.
- [69] W. Walukiewicz, J. Lagowski, L. Jastrzebski, and H. C. Gatos, "Minority-carrier mobility in *p*-type GaAs," *J. Appl. Phys.*, vol. 50, pp. 5040-5042, 1979.

- [70] J. E. Sutherland and J. R. Hauser, "A computer analysis of heterostructure and graded composition solar cells," *IEEE Trans. Electron Dev.*, vol. ED-24, pp. 363-372, 1977.
- [71] S. C. Eisenstat, M. C. Gursky, M. H. Schultz, and A. H. Scherman, "The Yale sparse matrix package 1: The symmetric codes," *Int. J. Numer. Meth. Eng.*, vol. 18, pp. 1145-1151, 1982.
- [72] S. C. Eisenstat, M. C. Gursky, M. H. Schultz, and A. H. Scherman, "The Yale sparse matrix package 2: The nonsymmetric codes," Tech. Rep. 114, Yale University, 1977.
- [73] H. Rutishauser, "Simultaneous iteration method for symmetric matrices," *Numer. Math.*, vol. 16, pp. 205-223, 1970.
- [74] G. A. Kosinovsky, "Solution of the Helmholtz equation for semiconductor lasers," M. S. thesis, Univ. of Illinois at Urbana-Champaign, 1990.
- [75] W. T. Tsang, "Extremely low threshold (AlGa)As graded-index waveguide separate-confinement heterostructure lasers grown by molecular beam epitaxy," *Appl. Phys. Lett.*, vol. 40, pp. 217-219, 1982.
- [76] S. D. Hersee, M. Krakowski, R. Blondeau, M. Baldy, B. de Crémoux, and J. P. Duchemin, "Abrupt OMVPE grown GaAs/AlGaAs heterojunctions," *J. Crystal Growth*, vol. 68, pp. 383-388, 1984.
- [77] N. K. Dutta, "Calculated threshold current of GaAs quantum well lasers," *J. Appl. Phys.*, vol. 53, pp. 7211-7214, 1982.
- [78] T. L. Paoli, "Modulation characteristics of cw laser diodes," in *IEEE Int. Electron Devices Meeting 1976, Tech. Dig.*, 1976, pp. 136-139.
- [79] M. S. Adler, "Accurate calculations of the forward drop and power dissipation in thyristors," *IEEE Trans. Electron Devices*, vol. ED-25, pp. 16-22, 1989.
- [80] B. R. Nag, *Electron Transport in Compound Semiconductors*. Berlin: Springer, 1980.
- [81] B. R. Nag and N. Chakravarti, "On a simplified form of Kane's dispersion relation for semiconductors," *Phys. Status Solidi B*, vol. 71, pp. K45-K48, 1975.
- [82] E. G. S. Paige, in *The Electrical Conductivity of Germanium*, A. F. Gibson and R. G. Burgess, Eds. London: Heywood, 1964.
- [83] C. Jacoboni and L. Reggiani, "The Monte Carlo method for the solution of charge transport in semiconductors with applications to covalent materials," *Rev. Mod. Phys.*, vol. 55, pp. 645-705, 1983.

- [84] K. Bløtekjær, "Transport equations for electrons in two-valley semiconductors," *IEEE Tran. Electron Devices*, vol. ED-17, pp. 38–47, 1970.
- [85] C. T. Wang, "A new set of semiconductor equations for computer simulation of submicron devices," *Solid-State Electron.*, vol. 28, pp. 783–788, 1985.
- [86] E. M. Azoff, "Energy transport numerical simulation of graded AlGaAs/GaAs heterojunction bipolar transistor," *Tran. Electron Devices*, vol. ED-36, pp. 609–616, 1989.
- [87] S. Chapman and T. G. Cowling, *The Mathematical Theory of Non-Uniform Gases*. London: Cambridge University, 1939. (The *first* and *second* approximate solutions of Enskog are named later the *zeroth* and *first* solutions of Enskog, respectively, in more modern books. We followed the latter practice.)
- [88] K. Seeger, *Semiconductor Physics*, 4th ed. Berlin: Springer, 1989.
- [89] Y. Ohno, "Electron viscosity effects on electron drift velocity in silicon MOS inversion layers," in *IEEE Int. Electron Devices Meeting 89 Tech. Dig.*, 1989, pp. 319–322.
- [90] S. P. Gaur and D. H. Navon, "Two-dimensional carrier flow in a transistor structure under nonisothermal conditions," *IEEE Tran. Electron Devices*, vol. ED-23, pp. 50–57, 1976.
- [91] S. M. Sze, *Physics of Semiconductor Devices*, 2nd ed. New York: John Wiley, 1981.
- [92] J. S. Blakemore, "Approximations for Fermi-Dirac integrals, especially the function $\mathcal{F}_{1/2}(\eta)$ used to describe electron density in a semiconductor," *Solid-State Electron.*, vol. 25, pp. 1067–1076, 1982.

VITA

Ghie Hugh Song was born in Seoul, Korea, in 1957. He received the B.S. degree with honors in electronic engineering from Seoul National University in 1980, and the M.S. degree in electrical engineering from the Korea Advanced Institute of Science in 1982. During 1982-1985, he was employed by the Applied Optics Laboratory at the Korea Institute of Science and Technology as a member of the technical staff, working on integrated optics and birefringence characteristics of optical fibers. In 1985, he enrolled in the Ph. D. program in the Department of Electrical and Computer Engineering at the University of Illinois at Urbana-Champaign.